



*Facultad
de
Ciencias*

**ESTUDIO DE SENSORES DE
RADIACIÓN DE SILICIO CON
GANANCIA INTEGRADA**

**(Study of Silicon
Radiation Sensors with
integrated gain)**

**Trabajo de Fin de Máster
para acceder al**

**MÁSTER EN FÍSICA, INSTRUMENTACIÓN Y
MEDIOAMBIENTE**

Autor: Andrea García Alonso

Director: Gervasio Gómez

Co-director: Iván Vila Álvarez

Septiembre - 2017

Estudio de sensores de radiación de silicio con ganancia integrada

Alumno: Andrea García Alonso

Documento: Trabajo de Fin de Máster

Idioma: Inglés

Máster: Física, Instrumentación y Medioambiente

Año académico: 2016-2017

Dirección: Gervasio Gómez. Iván Vila Álvarez

Fecha de realización: Febrero-Julio 2017

Palabras clave: LGAD | iLGAD | sensor | detector de silicio | física de partículas | física de altas energías | ganancia | microstrip | multiplicación

Resumen

En el presente trabajo de fin de máster, se realiza una caracterización completa de nuevos sensores de silicio con ganancia integrada: LGAD e iLGAD. Para ello, se detallan los principios básicos de su funcionamiento, y se estudian las propiedades eléctricas y su respuesta a partículas ionizantes, tanto de fuente radiactiva, como de piones y protones altamente energéticos. Se estudian la distribución de carga y la eficiencia, como función del voltaje aplicado y de la temperatura. Se efectúan estudios equivalentes con láser infrarrojo, estableciéndose la correspondiente comparativa entre los diferentes tipos de fuente de radiación. Se lleva a cabo un estudio de la ganancia y se proponen aplicaciones futuras.

Key words: LGAD | iLGAD | sensor | silicon detector | particle physics | high energy physics | gain | microstrip | multiplication

Abstract

The present master dissertation studies new silicon sensors with integrated gain: LGAD and iLGAD. In order to achieve this goal, their basic functioning principles are explained and their electric properties and response to ionizing particles are studied. The radiation sources which have been used are highly energized pions and protons and a ^{90}Sr radioactive source. Charge distribution and efficiency as functions of the applied bias voltage and temperature are studied. Similar studies are also performed using an infrared laser source, establishing the corresponding comparative between the different types of radioactive sources. A gain study is carried out and future applications are proposed.

Table of contents

Abstract	3
Introduction	5
Chapter 1: Silicon detectors in Elementary Particle Physics	6
1.1 Semiconductor ionizing sensors.....	8
1.2 PN junction	11
1.3 Current induction	14
1.4 Silicon detectors	15
Chapter 2: LGAD and iLGAD. Physical properties and functioning	16
2.1 Avalanche Photo-Diodes	17
2.2 LGAD sensor	18
2.3 iLGAD sensor	20
Chapter 3: Experimental setup for the characterisation	22
3.1 Measurement system: ALIBAVA	22
3.2 Test Beam tracking setup.....	24
3.3 Radioactive source setup	26
3.4 Infrared laser setup	27
3.5 Signal Reconstruction.....	27
3.6 Calibration	31
3.7 Data processing codes.....	33
Chapter 4: Characterisation results and discussion	34
4.1 Test Beam	34
4.2 Radioactive source	40
4.3 Infrared laser	43
4.4 Comparison between radiation sources	45
Conclusions and outlook	47
References.....	48

Introduction

In High Energy Physics experiments, Silicon based sensors are becoming an essential element for detection. Silicon constitutes a versatile semiconductor material for charged particle detection, tracking, momentum measurement, calorimetry, vertexing, particle identification and muon detection.

Nowadays, projected future experiments require high momentum resolution, like the International Large Detector or ILD for the future International Linear Collider (ILC) which will detect the debris of collisions of electrons and positrons at energies of 500 GeV which could rise to 1 TeV. Its physics program will extend and complement the one of the Large Hadron Collider or LHC. It requires precision and places great demands on the detector performance. Excellent calorimetry and tracking are needed for event and particle reconstruction. Moreover, efficient reconstruction of secondary vertices and high momentum resolution for charged particles are essential for this possible ILC detector [1].

There is also another detector design for the ILD: the SiD Detector, based on a robust silicon vertex and tracking system, combined with a 5 T central solenoidal field, to achieve an excellent momentum resolution [2].

This work is developed in this context, studying new position sensitive devices for tracking, with the objective of characterising new silicon detectors with intrinsic gain based on avalanche photodiodes (APD). These new detectors have the advantage of being quite thin while collecting high signals, decreasing the multiple scattering, achieving an almost undeflected particle track.

The goal of this academic work is to provide a proof of concept of the first segmented sensors with gain: the Low Gain Avalanche Diode or LGAD and the inverse-LGAD or iLGAD detectors. These are the first sensors of their type and were fabricated by the IMB-CNM (Instituto de Microelectrónica de Barcelona - Centro Nacional de Microelectrónica).

This thesis starts with an introduction to sensors in chapter 1: semiconductor principles, PN junction basis and silicon detectors information is provided. Chapter 2 explains the LGAD and iLGAD sensors structure and the physical processes which produce the measurable signals. In chapter 3 the readout process and setup is addressed. In order to do this, it starts showing the different contributions to the measurable signal: pedestals, noise, calibrations, etc. Then, the measuring setup is explained in detail for three radiation sources: a pion/proton beam, ^{90}Sr radioactive source and infrared laser. In addition, this chapter shows how the signal is reconstructed from data and how the readout hardware is calibrated. In its last part, the programming codes for the data processing are explained. Finally, in chapter 4, the sensors are characterised. The analyzed data, results of the three types of measurements (Test Beam, radioactive source and infrared laser), are compared and discussed. Results and analysis are tested demonstrating that LGADs and iLGADs are a new type of detector with a great potential and future in tracking experiments in particle physics.

Chapter 1: Silicon detectors in Elementary Particle Physics

Elementary Particle Physics pursues ambitious goals as a global theory able to unify all existing processes, discover new phenomena or explain the origin of the universe, find new ways of treating illnesses, among many others. In order to achieve them, matter is subjected to extreme conditions in collider experiments: high velocities, high energies, energetic collisions, ultrafast readout, etc. These extreme conditions require unique hardware and software developments.

Particle detector systems are ensembles of several layers of sub-detectors, each one designed to measure specific properties of particles. The following layers can be found in a typical detector system: tracking devices which reveal the path followed by particles; calorimeters which stop, absorb and measure the energy of the particles; or particle-identification detectors which identify the kind of generated particles during a collision. During a particle collision, resulting particles travel in all directions, so in colliding beam experiments, the detectors must cover the entire interaction region, and this is the reason why they are called “ 4π detectors” [3].

The most common detection techniques are based on ionization. On the one hand, when it is necessary to cover large volumes or areas, the detectors whose use has been more extended are gaseous ionization detectors. These detectors measure the current flow caused by the resulting electrons and ions when a particle with enough energy to ionize a gas atom or molecule traverses them. On the other hand, when compactness, precision and speed are required properties for detection, the most used detectors are the silicon-based position sensitive detectors.

Silicon detectors have many advantages compared to other types. They are compact, which constitutes a goal when designing a detector; their cost is not very high, silicon is the second most plentiful element in the crust of the Earth; they can easily be machined into microscopic strips or pixels making them the most accurate detectors in terms of spatial resolution. Moreover, silicon detectors have a high quantum efficiency in the visible part of the spectrum and they are insensitive to high magnetic fields [3].

Besides, in order to create an electron-hole pair, the energy loss needed in silicon is only about 3.6 eV, whereas the ionization energy in gases is about 15 eV or higher. Additionally, the ionization density in silicon is several orders of magnitude higher. While in silicon 7.6×10^5 electron-hole pairs per centimetre are created when a minimum ionizing particle (mip) enters in the bulk, only around 10^2 ionized molecules are created in gases [3].

In HEP experiments, it is crucial to measure the momentum of charged particles. One method to calculate this magnitude of a particle is to track its path through a magnetic field and measure its curvature. As an example, the CMS tracker can reconstruct the paths of high-energy muons, electrons and hadrons, and it can also find tracks coming from the decay of short-lived particles, by finding their positions at a number of key points. The tracker needs to record particle paths accurately, and at the same time be lightweight so as to disturb the particle as little as possible. It does this by taking position measurements so accurate that tracks can be reliably reconstructed using just a few measurement points. Each measurement of the CMS tracker is accurate to 10 μm . Figure 1.1 shows a typical arrangement of sensor modules covering the central region of a detector in several concentric layers.

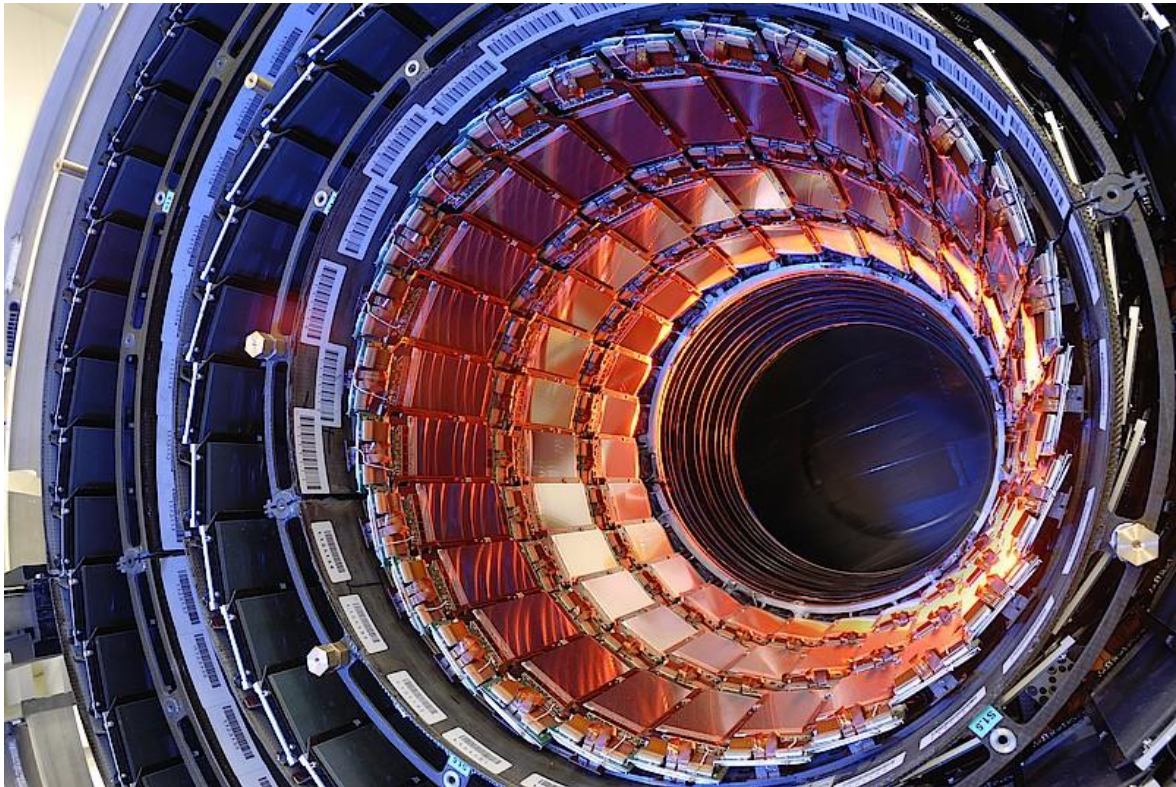


Figure 1.1. Typical arrangement of sensor modules covering the central region of a detector in several concentric layers [4].

For CMS, the sensors themselves are p-on-n silicon microstrip detectors and their geometry varies depending on their position. The sensor thickness varies from 320 to 500 μm and the inter-strip distance varies from 80 to 205 μm . Charged particles travelling across a magnetic field bend due to the Lorentz force, and the radius of curvature R is proportional to p/B , where p is the momentum transverse to the magnetic field and B is the magnetic field intensity. In a tracker only several spatial points can be measured, and R is calculated from the deviation from a straight line or sagitta, which is proportional to L^2/R , where L is the track length. The relative momentum resolution can be expressed as Eq. (1).

$$\frac{\delta p}{p} = \frac{8p}{0.3B \cdot L^2} \cdot \delta y; \quad (1)$$

where dy is the spatial resolution of each measured point. It is important to notice that the relative momentum error is proportional to the momentum itself, and inversely proportional to the magnetic field intensity and to the square of the travelled length. A good tracker must therefore aim to maximize L , B , the measured number of points and their individual resolution (minimize strip pitch).

In addition, particles moving through the detector suffer electromagnetic collisions which alter their trajectories in a random way. This stochastic process is called Multiple Scattering and it is proportional to $1/p$ (particles with low momentum scatter more), and it degrades momentum resolution. Multiple scattering increases with the number of radiation lengths X_0 traversed by the particle. The radiation length of a material is the distance after which a high energy electron has a fraction $1/e$ of its original energy. The radiation length of Silicon is 9.37 cm. The number of radiation lengths traversed depends both on the material type and thickness. In order to minimize multiple scattering, trackers aim to minimize the total material thickness. One advantage of using LGADs and iLGADs for tracking purposes is that they can be fabricated with very small thicknesses and, owing to their intrinsic gain, still maintain a significant amount of signal. They are therefore ideal for high precision tracking applications.

In silicon radiation detectors the three main elements which can be found are: a semiconductor ionizing medium, an electric field generated by a PN junction and a induced current in the electrodes. In this chapter, the basic principles of semiconductors, PN junction, diodes and current induction are explained, in order to introduce the distinctive physics features of silicon detectors and consequently, LGADs and iLGADs.

1.1 Semiconductor ionizing sensors

In an ionizing radiation detector the main component is the ionizing medium, constituted by a silicon semiconductor. The incident radiation produces here electron-hole pairs which induce a signal in the electrodes.

When a minimum ionizing particle or mip traverses a silicon detector it loses energy due to ionization. While it is travelling through silicon atoms, it tends to take electrons from their highest energy levels, ionizing them and consequently creating pairs of electron and hole [5]. When a photon travels through the silicon detector, if it is absorbed, an electron will be liberated, leaving a vacancy or positive charge, called hole. In both situations, electrons are excited and said to be promoted to the conduction band, leaving holes in the valence band. These 'free' charges move under the influence of an electric field and induce a measureable signal [3].

Silicon semiconductor is a medium composed by a periodic arrangement of atoms forming a crystalline structure. These atoms are so close that their outer shell atomic levels form an energy band structure with regions of many closely spaced levels,

considered as continuum, and a forbidden energy band gap or lack of available levels [6]. This energy gap separates the conduction and valence bands. The valence band is the range of levels where electrons remain at absolute zero temperature, while the conduction band is formed by upper levels where an electron can be promoted and generate electric current, due to the fact of being so far from the nucleus that binding is weak and they can freely move. The Fermi level or chemical potential is found between these two bands. Since the energy gap is small, adding impurities (doping the semiconductor by replacing atoms of the material with atoms of another element with different valence and similar size) in order to change its conductivity is possible.

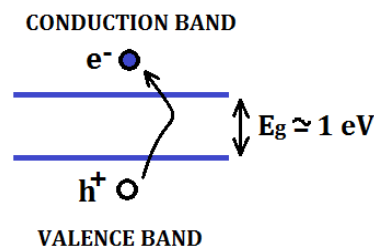


Figure 1.2. Semiconductor band schema. Energy of the band gap between the valence and conduction bands is low. Thermal excitation makes electrons promote to the conduction band, leaving holes in the valence band.

In a conductor material these two bands are quite close or even joined, allowing electrons to move from one to another involving a low energy exchange, as shown in Figure 1.3. The electron density in the conduction band is significant so electric current is conducted. On the other hand, in an insulator these bands are separated by a large band gap, whose energy E_g is around 4 eV or higher. Therefore, this large separation implies that electrons fill valence band and rarely promote to conduction band, so almost no electrons are free and electric current is not conducted.

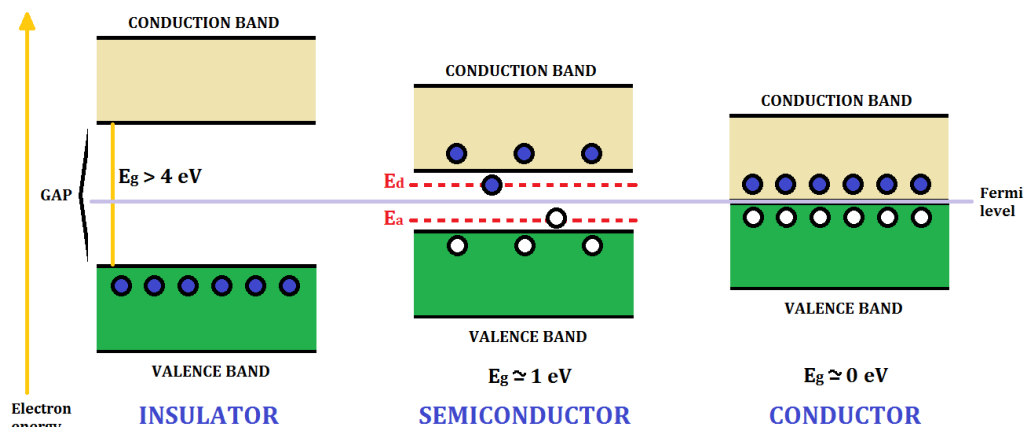


Figure 1.3. Band schema of an insulator, semiconductor and conductor. Energy gap is high in insulators ($E_g > 4$ eV), but low or null in conductors. In semiconductors, new energy levels (donor or acceptor impurities) make possible more transitions through the gap. Blue circles are electrons, and white holes.

However, in semiconductors the band gap constitutes the case between these two. Moreover, its magnitude can be changed adding donor or acceptor impurities, creating new energy levels (E_d and E_a respectively in Figure 1.3) between both bands.

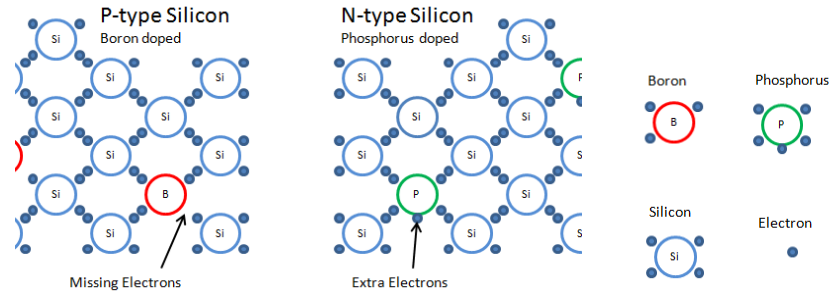


Figure 1.5. Crystalline structure of Silicon when doped with an element of Group III like boron (left, P-type) or Group V like phosphorus (right, N-type) [7].

Silicon atomic number is 14, it is a semiconductor from Group IV and presents four valence electrons. It crystallizes forming covalent bonds with its neighbouring atoms. If in a silicon material one atom is replaced with a boron atom, which only has three valence electrons, there is an incomplete bond, a lack of electrons, so there is an extra positive charge, a hole, as shown in Figure 1.5. The doping is positive, the charge carriers are holes: this is a P-type semiconductor. However, if the silicon atom is replaced with a phosphorus one, which has five valence electrons, there is an extra electron from this new element which is not forming a bond and it is free to move around. The doping is negative, the charge carriers are electrons: this is an N-type semiconductor, as can be seen in Figure 1.5. The sensors studied in this work use boron impurities in the P type zone, and phosphorus in the N type zone.

Once the silicon has been doped, electrons from donor levels with E_d energy (represented with red line in Figure 1.3) can be promoted to conduction band, contributing to the conduction process. This new levels are electronic available states which do not constitute bands. Moreover, holes from acceptor levels with E_a energy can accept electrons from the valence band. The impurities move the Fermi level of the semiconductor from its central position, to a lower energy in the case of acceptor impurities, and to a higher one in the case of donors.

The conduction band occupation probability $P_{ocup}(E)$ is proportional to the temperature and it is given by the Fermi-Dirac distribution (2). The density of carriers depends on the temperature T and Fermi level.

$$P_{ocup}(E) = \frac{1}{e^{-(\mu-E)/kT} + 1} \quad (2)$$

Semiconductors constitute a class of material used as the base of many electronic devices such as transistors, and whose behaviour is positioned between insulators and conductors, depending on external factors. Semiconductor resistivity is found between insulators (on the order of 10^{12} - $10^{16} \Omega \cdot m$) and conductors (on the order of $10^{-8} \Omega \cdot m$) and is highly temperature dependent. The resistivity is a measure of how strongly a material opposes the flow of electric current, or the difficulty which an electric current can pass through the material under the influence of an electric field. Resistivity, and consequently its reciprocal magnitude conductivity, can be controlled by varying temperature or doping concentration in the semiconductor [8] [9] [10].

1.2 PN junction

When bringing together a P-type and an N-type semiconductor, through a metallurgical boundary, a PN junction is created. This constitutes the base of almost all current electronic devices, as we can find in diodes or rectifiers and transistors.

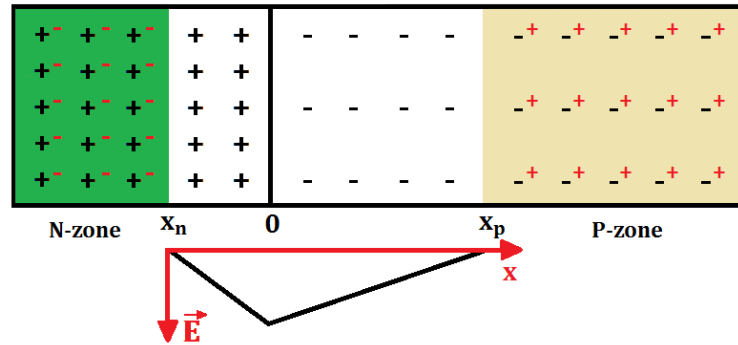


Figure 1.4. PN junction diagram and electric field behaviour. The electric field generated in the depletion region (space between x_n and x_p) is generated by the moved charge carriers which exchanged positions due to diffusion. It reaches its maximum value at the junction.

The P zone is joined with the N zone as Figure 1.4 shows, where the black line separation represents the metallurgical boundary. Generally one element of the junction can be more doped than the other. In Figure 1.4 the N zone is highly doped ($N_d \approx 10^{16} \text{ cm}^{-3}$) and has a small width, while the P zone has lower doping concentration ($N_a \approx 10^{12} \text{ cm}^{-3}$) and is wider. The reason why impurity densities and volumes are different in each zone resides in the fact that low voltages are required in order to deplete the entire bulk. The neutrality condition, given by Eq. (3), is satisfied.

$$N_a \cdot x_p = N_d \cdot x_n \quad (3)$$

Both doped zones own charge carriers (represented in Figure 1.4 with red plus and minus symbols) susceptible to reorganize along the junction through diffusion movements. For simplicity, it is usually assumed that donor and acceptor densities in each part are uniform and the junction is abrupt, so the doping densities are completely separated.

The free charges (extra electrons in the N-zone and holes in the P-zone) try to occupy all the available space, creating a diffusion current due to the concentration difference between the two zones. Electrons and holes recombine near the junction creating a region depleted of free charge, called 'depleted region', where only ionized donor or acceptor impurities remain. However, the nuclei of the donor and acceptor atoms are fixed in the crystalline lattice and cannot move. Therefore an electric field, whose definition is given by Eq. (5), builds up and creates a drift current which opposes the diffusion process. This field is obtained from the Poisson equation (4) and has its maximum value in the borderline between the two zones and linearly decreases with distance to this region. When the drift and diffusion currents are equal (but opposite) the depletion process reaches the equilibrium and the depletion region stops growing.

This configuration constitutes a silicon controlled rectifier (SCR) due to the fact that it can conduct current only in one direction when applying an external bias.

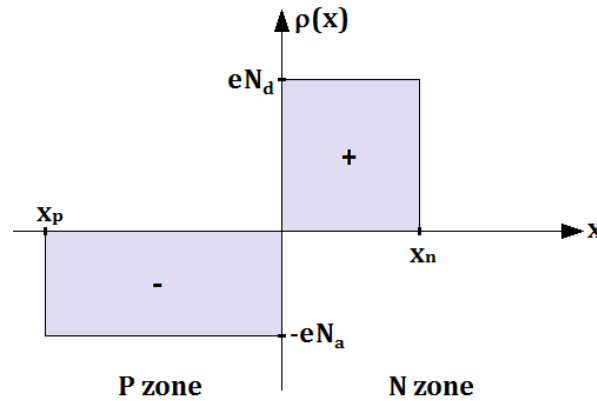


Figure 1.6. Space charge distribution. Neutrality condition given by Eq. (3) is satisfied.

The constant electric field in this crystalline structure depends on the charge space (represented in Figure 1.6) (acceptor and donor space distributions). From Poisson equation (4) applied to each zone of the PN junction and after an integration process, the electric field expression (5) is obtained.

$$\frac{d^2\phi(x)}{dx^2} = \frac{-\rho(x)}{\epsilon_s} \Rightarrow \frac{d^2\phi(x)}{dx^2} = \begin{cases} \frac{+e \cdot N_a}{\epsilon_s} & \text{for } x_p < x < 0 \\ \frac{-e \cdot N_d}{\epsilon_s} & \text{for } 0 < x < x_n \end{cases} \quad (4)$$

$$E(x) = \begin{cases} \frac{-e \cdot N_a}{\epsilon_s} (x + x_p) + C_1 & \text{for } x_p < x < 0 \\ \frac{e \cdot N_d}{\epsilon_s} (x_n - x) + C_2 & \text{for } 0 < x < x_n \end{cases} \quad (5)$$

Where ϵ_s constitutes the relative permittivity of silicon, whose value is around 11.7.

When a minimum ionizing particle (mip) traverses the sensor, it creates electron-hole pairs along its path. In silicon, the number of created pairs is around 76 per micron, as mentioned earlier. Outside the depleted region, the charge carrier concentration is many orders of magnitude larger than any free charge created by ionization, and the electric field is low. However, in the depleted region, the only charge carriers are those resulting from ionization and the electric field is higher, so the pairs created in this zone can travel inducing a detectable current on the electrodes.

This is the reason why the depletion zone is the sensitive part of a sensor, so it should be the widest possible in order to get higher signals and efficiency and larger detection coverage. If an external voltage is applied in reverse bias (a positive voltage is applied at the N-zone and a negative one at the P-zone), the depletion zone increases, until the

sensor is completely depleted and its efficiency is the maximum which can be achieved. The 'full depletion' voltage is the value of the applied voltage when the depleted zone occupies the entire volume of the sensor. This magnitude is essential when characterising a sensor because it indicates the minimum voltage from which it works best.

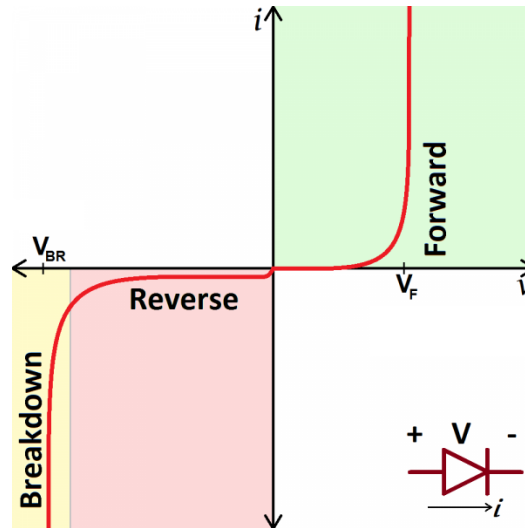


Figure 1.7. I-V curve for a diode [11].

Now, the current flux J inside the sensor is due to the sum of the diffusion current and the recombination of the minority carriers. At constant temperature, its value is constant along the bulk (between x_p and x_n), and it is defined by Eq. (6). Its response with voltage, which is similar to a diode, is shown in Figure 1.7. At 300K, the factor kT/e is 26 mV.

When working in reverse bias (working conditions of LGADs and iLGADs, as it will be explained later) the exponential term quickly becomes negligible. The resulting current is called dark current, and is approximately constant and very small. This current depends only on the temperature and the quality of the diode material.

On the other hand, applying a forward bias, electric conduction is possible from a voltage value for which the electrons can overtake the intrinsic voltage step.

$$J_{total} = \frac{e \cdot L_p \cdot D_n \cdot n_{no} + e \cdot L_n \cdot D_p \cdot p_{no}}{L_n \cdot L_p} \cdot [\exp(e \cdot V_a / k \cdot T) - 1] \quad (6)$$

In Eq. (6), L represents the diffusion longitude of each type of carrier, D is the diffusion coefficient, and n and p are the carrier densities. The rest of magnitudes are the electron charge e , temperature T and Boltzmann constant k .

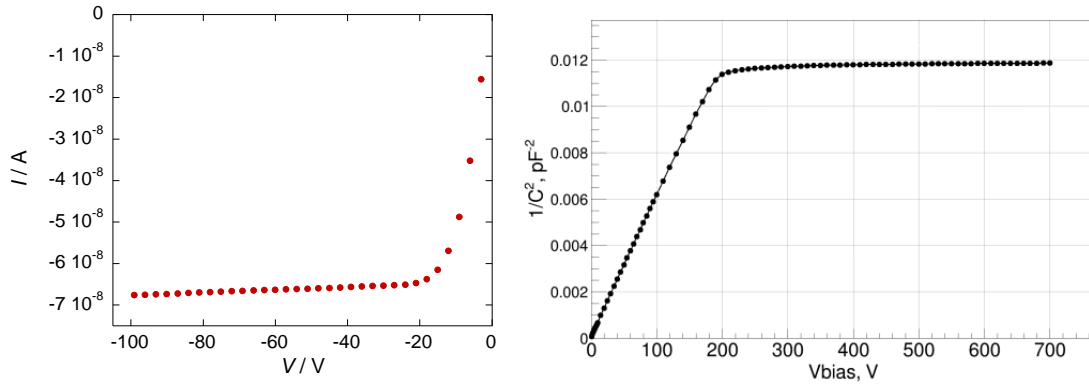


Figure 1.8. I-V and C-V measurements for a diode in reverse bias.

Figure 1.8 (left) shows an I-V curve measurement of a diode in reverse bias, done in the laboratory of IFCA. Notice the similar behaviour shown in Figure 1.7 before breakdown voltage. If the electric field is increased several orders of magnitude, breakdown occurs ($E > 10^5 \text{ V}\cdot\text{cm}^{-1}$). At this point, free charges are so accelerated that can ionize bounded electrons and generate new electron-hole pairs in the depleted region. This process is called impact ionization. Electric current quickly increases tending to infinite, so the detector is commonly irreversibly damaged [12].

The electric field in the depleted region from Eq. (5) is proportional to the distance x from the junction. Since the electric field is the gradient of the potential, the depleted region in a diode increases as the square root of the bias voltage. The capacitance C in a diode of area A depleted to a thickness d is $\epsilon A/d$, and therefore it decreases as the square root of the bias voltage until the diode is fully depleted. At this point, the capacitance reaches a minimum value and remains constant. Figure 1.8 (right) shows $1/C^2$ versus bias voltage. As expected, $1/C^2$ increases linearly until the depletion voltage is reached, around 200 V, and remains constant afterwards.

1.3 Current induction

The current induced in an electrode is due to the instantaneous change of electrostatic flux lines which end on the electrode, and not to the amount of charge collected by the electrode per second. The induced current in each electrode is defined by Ramo Theorem, which is shown in Eq. (7), and makes possible to calculate the instantaneous electric current induced by a charge moving near an electrode. The induced current depends on the charge q of the carrier, voltage V_0 , weighting field E_n^w on the electrode n and carrier velocity v which depends on the real electric field according to $\vec{v} = \mu\vec{E}$.

$$I_n(t) = \frac{-q}{V_0} \cdot \vec{E}_n^w(x(t)) \cdot \vec{v}(t) \quad (7)$$

The weighting field E_n^w at electrode n is not the real field but a mathematical value obtained when assuming charge removed, given electrode raised to unit potential ($V_0 = 1 \text{ V}$), and all other conductors grounded. The weighting field gives a magnitude of the induction capacity of each electrode.

1.4 Silicon detectors

The main objective of most detectors in high energy physics is to measure the energy and position of the incident radiation or particle.

Generated ionization inside a silicon semiconductor is proportional to the energy loss of the incident radiation, so energy is easy to measure thanks to the collected charge on the electrodes. The equivalence between the number of ADC counts registered by the readout setup and the charge as a number of electrons is directly found with a calibration measurement.

However, the position characterisation is more complex, because it is necessary to recognize the region inside the sensible volume of the detector where the charge generation happened. In order to achieve this goal, the collector electrode of one detector pad or junction diode with a reverse bias is discontinuously implanted forming many sub-electrodes. The most common position sensitive sensors are strip and pixel sensors [12].

Strip sensors can localise particles in one direction because they are formed by strips or narrow lines, so the impact region of a particle passing through it can be determined on one of the multiple strips. Additionally, in order to get information in two dimensions, photolithographic techniques are used to implant doping impurities in microscopic pixels.

However, silicon detectors have a problem to deal with when they have been exposed to radiation for a long period: defects induced by radiation damage change the electric field and energy band structure and create trapping centres for charge carriers. It is then hard to discern the signal produced by the incident radiation from the noise. Additionally, the depletion voltage and dark current increase, and lower temperatures are required in order to operate them safely.

Chapter 2: LGAD and iLGAD. Physical properties and functioning

For high precision detectors, silicon sensors should be fabricated as thin as possible to minimize scattering, but this comes at the price of a reduced signal, so the signal to noise ratio gets worse and measurements become less efficient. In order to correct these issues one solution consists in amplifying the signal. This is multiplying the collected charge while maintaining its proportionality relation with the energy lost by the incident radiation.

LGAD and iLGAD detectors are new sensors based on APD (Avalanche Photo-Diodes) which implement charge multiplication.

Among their many advantages, a multiplication detector achieves a better signal to noise ratio. This way, low signals are detected so low energies can be studied and more sensitive detectors are obtained. In addition, finely segmented detectors improve space resolution [12]. A multiplication detector makes possible the following:

- ⊕ Better momentum resolution. Higher signals are obtained using less detection material, so the incident radiation path is less deviated.
- ⊕ Better time resolution. The time which the detector takes to form the signal after the arrival of the radiation is smaller, which means that the signal is quickly formed into a sharp pulse with a rising flank close to vertical [6].

The main difference between the new silicon sensors with integrated gain LGAD and iLGAD is that while LGAD is an n-on-p sensor, iLGAD is a p-on-p sensor. Another important difference is that the multiplication layer is segmented for the LGAD, but continuous for the iLGAD, as will be explained later.

This chapter describes the properties and operating principles of these sensors, starting with a brief introduction to avalanche photodiodes and the multiplication process. Then LGADs structure and functioning is treated, ending with iLGADs and showing the similarities and differences between each kind of sensor.

2.1 Avalanche Photo-Diodes

The avalanche Photo-Diodes or APD are detectors which show an internal current gain when applying a high reverse bias voltage, before reaching the breakdown voltage. At this voltage, as before mentioned, charge carriers are so accelerated due to the intense electric field, that they can generate new electron-hole pairs from the crystalline structure of the semiconductor depleted region. Original carriers and the secondary ones are accelerated while staying in the high electric field region, and can generate new electron-hole pairs again, triggering an avalanche process which multiplies the collected charge carrier amount in both electrodes.

The difference between charge collection and electron-hole pair generation rates define the avalanche process duration. If the first one is higher, the ionization process decreases with time until the avalanche process is completely stopped. Nevertheless, if the pair generation is so high that carriers do not have enough time to be collected, the avalanche process is uncontrolled, increasing until breakdown.

These two cases define the two ways an APD detector can work. The first one constitutes the lineal mode where breakdown voltage is never reached. A great part of the generated charges can get out of the region with high electric field without increasing their velocity so much to create new pairs. The second way requires a setup capable of containing the avalanche. It constitutes the Geiger operation mode because it works similar to Geiger counters where number of events is measured, but not their intensity.

Linear mode is considered next, because its functioning is the base of LGAD and iLGAD sensors.

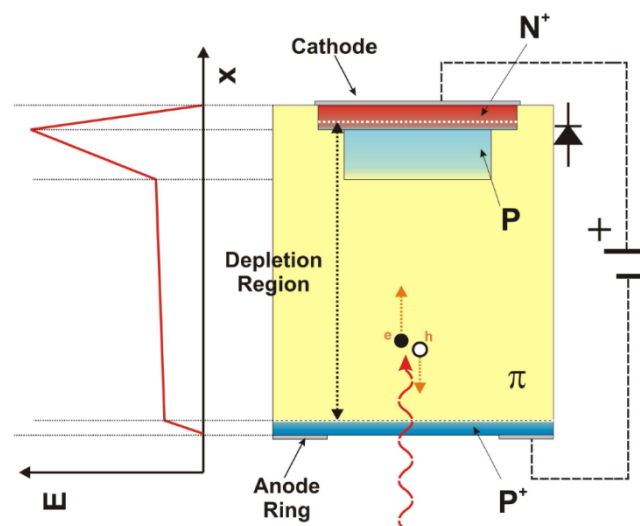


Figure 2.1. Schematic cross-section of an APD working in linear mode. Its electric field space distribution is represented on the left [12].

In Figure 2.1, an APD working in linear mode is represented. A PN junction with a highly doped narrow N-zone (N^+) and a wide doped P-zone, as the one explained in Section 1.2 is placed at the top part of a very low doped P-type bulk (the π -type region). On its bottom

part, a highly doped P-zone (P^+) is placed as an ohmic contact. A cathode collector is situated on the N^+ zone and an anode on the P^+ , and a reverse potential difference is applied between them. When red laser radiation, which highly interacts with silicon and penetrates only a few microns, enters through the P^+ anode, electron-hole pairs are created very close to this electrode. Consequently, the electrons travel to the electrode at positive voltage going through the entire bulk with an increasing velocity, while the holes are rapidly caught by the negative electrode. So the main current signal is due to the movement of electrons, as explained in Section 1.3. When they reach the P-zone, their velocity rapidly increases because of the large electric field, ionizing atoms of the multiplication layer and producing multiplication. These new carriers are electrons rapidly collected by the positive electrode and holes which travel to the negative one through the bulk, being the carriers which now contribute most to the signal.

The number of collected charges Q_c thanks to each initial carrier Q_0 (generated by the incident radiation) is a finite magnitude that can be expressed as a multiplication factor or gain G , as done in Eq. (8).

$$Q_c = G \cdot Q_0 \quad (8)$$

2.2 LGAD sensor

LGAD or Low Gain Avalanche Detector is a type of diode which makes use of impact multiplication in order to collect a bigger amount of electron-hole pairs when a mip enters its bulk. Consequently, signals are amplified without the need of external amplifiers.

An LGAD exploits the avalanche phenomenon of a reverse-biased PN junction. The sensor used in this thesis has a thickness of $285 \mu\text{m}$ and is composed by a double junction, as shown in Figure 2.2, there are 32 strips with a pitch (distance between strips) of $160 \mu\text{m}$.

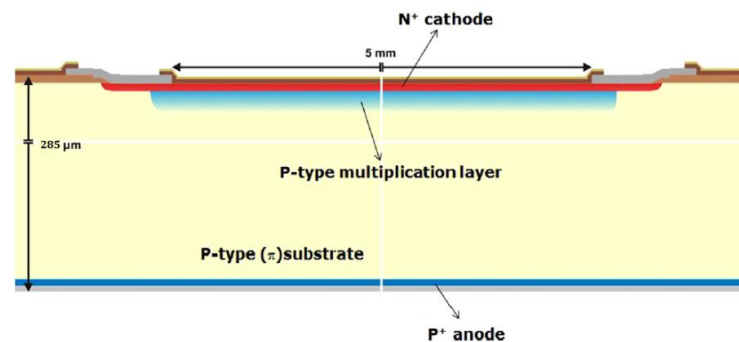


Figure 2.2. Cross-section of the core layout of LGAD. A p-type layer is diffused below the N^+ electrode to form the $N^+/P/P^+$ junction where the multiplication takes place [13].

A P-type substrate of doping density around 10^{18} and 10^{20} cm^{-3} constitutes the base layer. Over it, a low P-doped bulk (π -type substrate) is placed, constituting the bulk of the

sensor, so the main signal is generated here. On its top part, a highly doped P-type layer where the multiplication process happens is situated and joined to an N-type layer, creating a high electric field, due to the abrupt union of high density but oppositely charged impurities. In the junction between these N and P zones the highest electric field is found.

This sensor is called n-on-p. It collects negative charges (electrons) at the positively bias cathode. In our particular setup, the electrode has been implanted on the surface of the bulk forming the strips which give the high space resolution. These strips are connected to ground so the applied voltage at the anode is negative.

When doping the bulk of the material in order to create the strips, in a LGAD the multiplication layer itself is segmented, so this region discontinuously extends along the electrode surface, as can be seen in Figure 2.3.

Red laser has a penetration of only a few microns in silicon. Taking Figure 2.2 as reference, if illuminating with red laser from the bottom part, electron-hole pairs close to the P^+ anode surface are created. The electrons, attracted by the positive potential of the top cathode go up, until they arrive at the P-type multiplication layer. The path they travel is long ($285 \mu\text{m}$), so they induce a highly visible signal, in contrast to the holes, which are collected almost instantly by the anode and do not induce any significant signal. Once the electrons arrive to the P-type multiplication layer, the high electric field accelerates them to higher velocities until they arrive to the PN junction. Due to this acceleration, they become ionising, creating new electrons and holes which are redirected to the top cathode and bottom anode respectively. Consequently, the current due to each particle is multiplied. The signal due to the multiplication process is mainly due to multiplied holes travelling along the bulk, since multiplied electrons are quickly collected at the anode.

A real picture made with electronic microscope of an n-on-p microStrip LGAD is shown in Figure 2.3 (on the left) with its schematic representation (on the right).

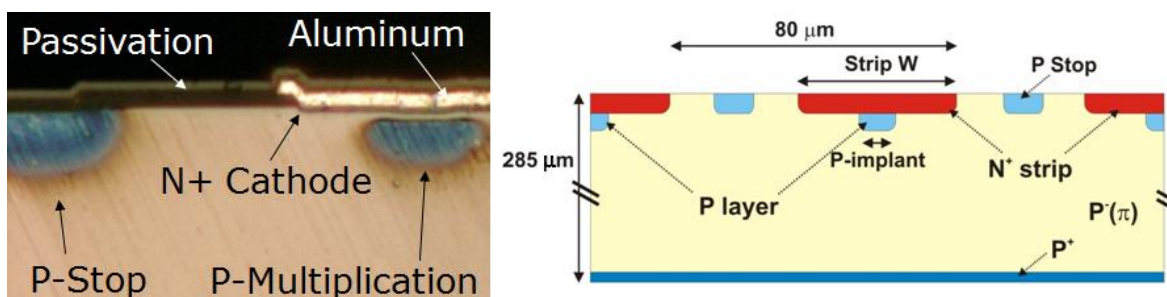


Figure 2.3. Real picture (left) and schema (right) of a microStrip LGAD.

In this Figure, the P stops are strip diffusions with doping opposite to the strips. Their objective is to separate strips electrically, by building a negative electric field which repels (or stops) electrons.

The shape of the signal for a red laser shining from the bottom as a function of time is shown in Figure 2.4. There is a sharp increase due to the original fast electrons which

ends when they arrive to the cathode. At sufficiently high voltage, electron-hole pairs are produced at the multiplication layer. The holes travel across the bulk inducing a second signal peak which appears after the primary peak and is less sharp due to a smaller hole mobility compared to electrons (about one third). Finally, it becomes zero when the holes reach the anode.

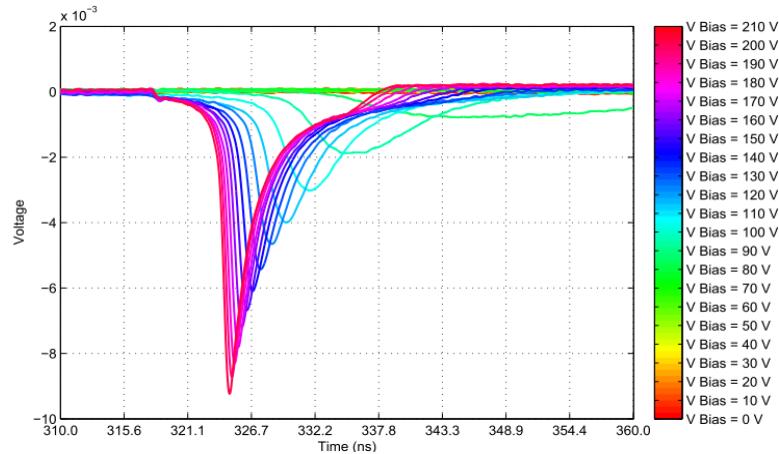


Figure 2.4. Signal distribution as a time function, for several bias voltages, in an LGAD. Electron injection from bottom side of the sensor with red laser [14].

In the LGAD charge profile analysis, two zones can be distinguished due to the contribution of charges which reach the collector electrode through the multiplication layer and the ones which do not, because the multiplication layer is segmented.

2.3 iLGAD sensor

The Inverse Low Gain Avalanche Detector or iLGAD is a p-on-p silicon sensor, as shown in Figure 2.5. It collects positive charges (holes) at the P-type collector electrode. The multiplication layer is not segmented, so the double contribution to the charge profile observed in the LGAD does not happen because essentially all charge carriers go through the multiplication layer.

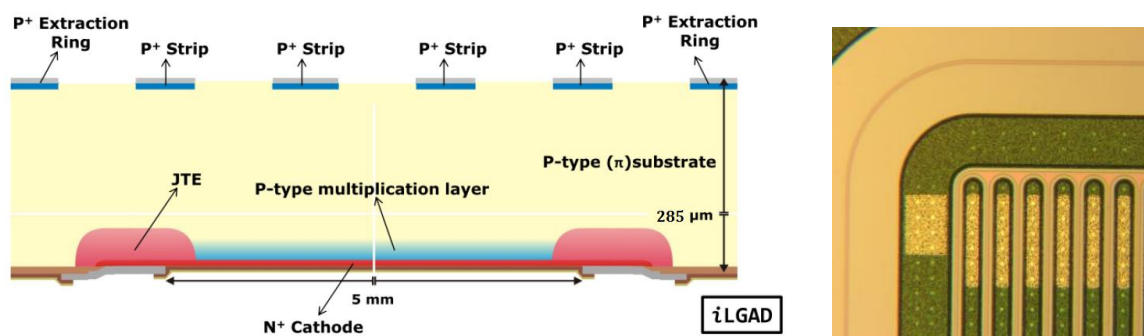


Figure 2.5. Cross-section of the core layout of iLGAD with a JTE structure protecting the junction edge termination. A p-type layer is diffused below the P⁺ electrode to form the P⁺/P/N⁺ junction where the multiplication takes place. On the right, a real picture of a strip iLGAD [15].

The iLGAD studied in here also has a thickness of 285 μm and 45 strips with a pitch of 160 μm (Figure 2.5 left is not drawn to scale). As can be seen in this figure, the strips are placed on the top part so the collector electrode is formed by multiple P⁺ diffusions, but the cathode and multiplication layer are on the bottom part. When characterising these sensors, the collector electrodes are connected to ground and the bottom electrode with the multiplication layer is set to a positive voltage. The resulting electric field is uniform all along the device volume guaranteeing the same signal amplification wherever a particle passes through the sensitive bulk.

In this case, the signal is dominated by holes travelling towards the segmented electrodes from the multiplication junction with the subsequent increase of the transient current pulse duration in comparison with LGAD (because hole mobility is about one third that of the electron). Applications of iLGAD range from tracking and timing applications, like determination of primary interaction vertex, to medical imaging.

In Figure 2.5, JTE means junction termination extension, which is an alternative design for the multiplication layer terminations which has been proposed for the LGAD and iLGAD detectors fabricated so far, which increases the breakdown voltage of the sensor. The JTE is an overlap of the main junction edge with an N-type diffusion of lower doping density, which extends deeper than the N⁺ electrode diffusion. The electric field distribution in a junction ended with it has a better uniformity, the voltage capability of the device significantly increases and the electric field peak at the junction edge is reduced below the critical value to trigger impact ionization, avoiding multiplication at the edge termination even for the highest voltage bias [13].

If the iLGAD is illuminated with red laser from its top part (segmented side), the induced current is initially governed by electrons travelling towards the multiplication layer (since holes are collected immediately at the negatively biased electrode). After the electrons reach the multiplication layer, secondary electron-hole pairs are generated, electrons are almost instantly collected by the cathode while holes travel towards the readout electrodes giving rise to a second contribution to the signal. Its representation as a time function is given in Figure 2.6.

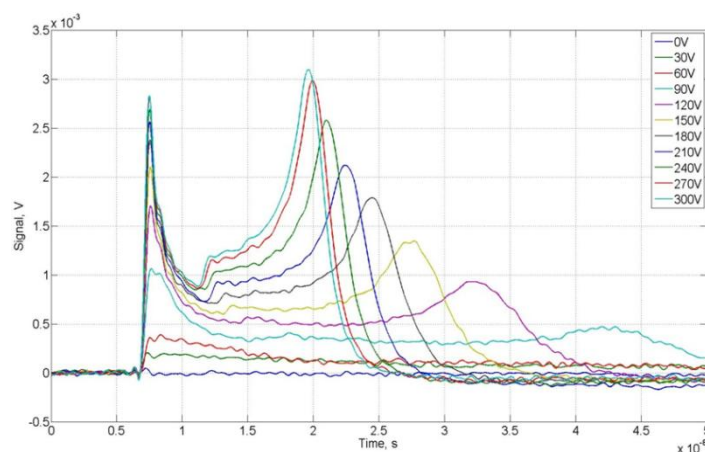


Figure 2.6. Signal distribution as a time function, for several applied voltages, in an iLGAD. Electron injection from top side of the sensor with red laser [15].

Chapter 3: Experimental setup for the characterisation

In this chapter, the data acquisition system (DAQ) used with LGADs and iLGADs, ALIBAVA systems [16], in order to characterise them and obtain all data from measurements is described in the first section. The components of the ALIBAVA system are explained: motherboards, daughterboards, beetles, etc.

When a sensor is connected to a readout setup and a particle crosses it, a trigger system fires the data acquisition, defining an event. All the information of that interaction is stored for processing. The reason why minimum ionizing particles (mips) (particles with a kinetic energy significantly greater than their rest mass) are used lies in the fact most hard scattered particles from beam collisions in high energy physics experiments are mips.

The measurement setup and data taking procedure for the three sources used to characterize sensors are shown.

Before reconstructing the signal in silicon sensors, it is important to explain its components. Concepts like pedestal, noise, signal to noise ratio, cluster and others which can be measured with the readout setup are studied here. In order to achieve this purpose, some plots obtained with the processing programs later explained are shown.

In the last part of this chapter, a brief overview about the software used for the offline data processing and a complete analysis strategy is discussed. Finally, the code improvements done in order to automate some fitting procedures are mentioned.

3.1 Measurement system: ALIBAVA

In order to make measurements with LGADs and iLGADs, a system called ALIBAVA has been used. ALIBAVA is a research instrument which allows the characterization of microstrip semiconductor radiation detectors. This system is composed by two main parts: the daughter board also called frontend or readout board, and the mother board, also known as backend or signal process board.

The frontend is directly connected to up to two sensors through its two beetles [17] or readout chips (ROC). A picture of this part of the system is provided in Figure 3.1. Each chip is a designed circuit which integrates 128 channels, each channel consisting of a low-noise charge-sensitive preamplifier, a pulse shaper, a buffer and an ADC. This way, when a particle goes through the sensor bulk, the low current signal registered by the sensor is

transformed into voltage and amplified enough so the next electronic device can measure it. The preamplifier transforms the low electric current generated by mips into a higher voltage pulse, introducing a certain gain.

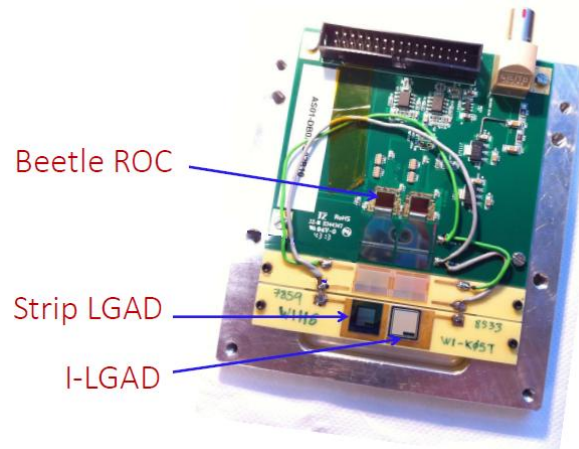


Figure 3.1. Picture of the interior of a daughter board, containing two sensors: LGAD and iLGAD to beetle 1 and 2 respectively [14].

All signal information is not saved due to the high volume of particles passing through the sensor and the limited capability of the readout system. The amount of charge generated per event is registered in each instant thanks to the shaper. It transforms the voltage step of the preamplifier into a fast decaying pulse with a peak height which is proportional to the charge at the front-end input. After registering a large number of mip events (around 10^5 events), the measured charges follow a Landau-Gaussian distribution. The position of the peak is the most probable value of the charge deposited by a mip. The buffer saves this data for a short period of time, until it is full and sends its contents to the mother board. Finally, a 10 bit ADC (Analog to Digital Converter) digitizes the analogical signal.

The second part, or mother board, is the part of the system which receives, transforms and arranges the signal in order to send it to the computer. Data is structured and headers are inserted. The mother board also manages the buffer, dead times and busy signal. It constitutes the brain of the readout system, the programmable electronics. It makes possible the correct synchronisation between all the readout system parts, delaying the fastest electronic devices in favour of the slowest, so the events recorded by ALIBAVA and other devices can be related. The time required by the ALIBAVA system to record data is defined by several factors which make the rest of the readout device wait. While the mother board is processing and sending data to the PC, it is not able to receive more data. When it finishes, the busy signal is not sent anymore and continues receiving data from the daughter board.

Nevertheless, this functioning will be explained in more detail in the following section, when the ALIBAVA system is implemented inside a bigger experiment.

3.2 Test Beam tracking setup

When very energetic ionizing particles, such as pions or protons, reach the LGAD or iLGAD surface, they go through the sensor, creating electron-hole pairs.

In order to study the response of the sensor when receiving mips, measurements with a beam of ionizing particles have been taken during a “Test Beam” (or TB). This kind of measurements are made at CERN, where it is possible to accelerate particles to almost the speed of light and direct them to the sensors. The energy of the protons and pions used in the experiment is 120 GeV.

The place where all the measurement are carried out is a particular part of the CERN accelerators: ‘the North Area’. Here, a part of the proton beam being accelerated in the Super Proton Synchrotron (SPS) is deflected by kicker magnets towards metallic targets. An additional system of beam optic magnets selects pions and protons from the target collisions and sends them towards the experimental areas. So in the North Area is where some experiments as this one can be done choosing different conditions. In the next figure a diagram of the CERN accelerators can be seen, and in particular, the North Area can be found almost in the centre of the LHC circumference.

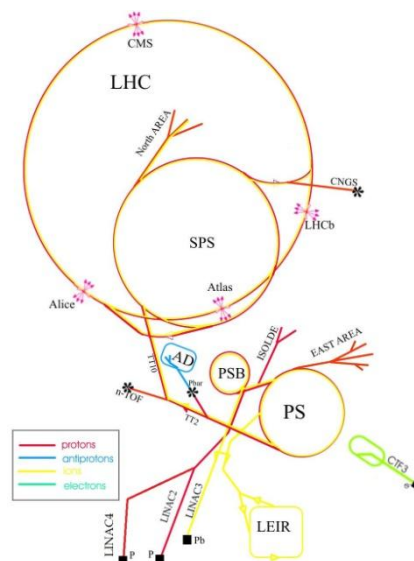


Figure 3.2. CERN accelerators diagram. Almost in the centre of the LHC is placed the North Area where the Test Beam measurements were made [18].

All the experimental devices are assembled inside a small part of an industrial unit. The beam pipe is situated in a lower part, surrounded by thick walls of lead which protect people from the radiation produced by the beam. In spite of this shielding, this place constitutes a supervised radiation area, so all the staff members working there have to wear a personal dosimeter, in order to measure how much radiation they are receiving and take protective measures to avoid radiological risks.

The measurement process is complex and the hardware needed is composed of several parts which are explained below.

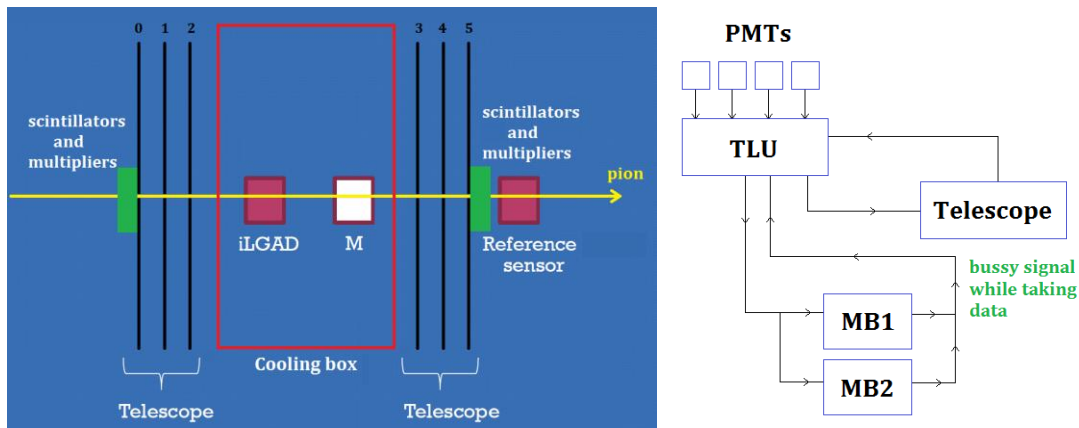


Figure 3.3. Diagrams of the two main parts of the Test Beam setup.
 a) Telescope planes, cooling box and sensors configuration transversal view.
 b) Electric circuit which represents the measurement system: trigger systems, SPS period, Trigger Unit, Telescope and ALIBAVA mother boards (MB1 y MB2).

The telescope unit is a device which allows us to reconstruct the trajectory of the particle which goes through the sensors. It is composed of two groups of three detection planes each. In the space between the two groups a cooling box is placed, where some sensors can be introduced and subjected to temperatures which can vary between -25°C and $+25^{\circ}\text{C}$.

One pair of scintillator-photomultiplier (PMT) detectors is situated before the plane 0 of the telescope, and another pair at the exit, after plane 5, see Figure 3.3a. When at least three of these PMTs register a signal, due to a particle passing, the trigger logic unit (TLU) sends a trigger command to the telescope and to each motherboard. Both the telescope and the ALIBAVA motherboards send a busy signal to the TLU while they are recording an event. When all busy signals are finished, the TLU can once again send a new trigger signal.

The ALIBAVA readout takes more time recording the data than the telescope. So when it receives the trigger signal, the TLU remains blocked and orders the telescope to wait and not take more measurements until it has finished. This makes possible to correlate ALIVABA and telescope events.

The accelerated particle traverses the entire setup with negligible scattering. The particle travels through both sensors and then through the second part of the telescope, to finally arrive to a reference sensor. The M sensor is another kind of sensor (a 3D pixel sensor) which was measured during the Test Beam, although it has no importance for this academic work. On the other hand, the reference sensor is a $300\ \mu\text{m}$ thick microstrip diode without gain whose function consists on making possible the gain quantification.

During the month of May 2017, another Test Beam was carried out, whose setup diagram is shown in Figure 3.4. Although the setup used in this case is quite similar, there were some minor differences. LGAD and iLGAD sensors were placed at room temperature, upstream of the cooling box. The telescope was composed by two front planes and three back planes, instead of three at each side of the cooling box. Although several sensors

were characterised, there were four motherboards available for measuring, so sensors took turns to be measured.

Data from both Test Beam experiments are going to be shown and discussed.

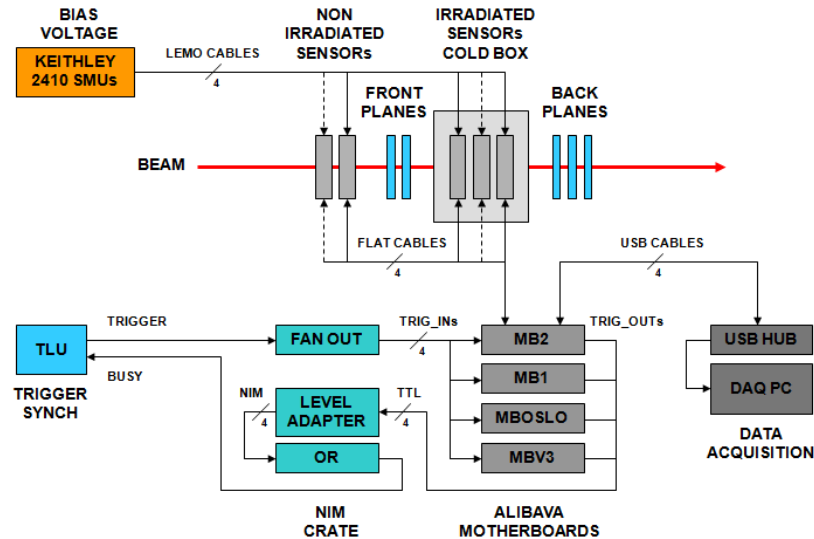


Figure 3.4. Complete diagram of the Test Beam setup carried out in May 2017.
Courtesy of Javier González Sánchez.

3.3 Radioactive source setup

Radioactive sources provide an alternative mechanism for characterizing sensors, in similar conditions to beam source, because it is another way of studying particle detection. While the source decay is happening, an ionizing particle is emitted, reaching the sensor and producing an effect comparable to test beam, although the energy and velocity of the particle is several order of magnitude less.

In this section, the response of a sensor when irradiated with a 90 Strontium source is studied. This radioactive element emits an electron when decaying into Yttrium, through β^- decay. The minimum ionizing particles which arrive to the detector are electrons with about 546 keV of maximum energy.

The way used to assess the effect of a radioactive source on sensors consists on placing the sensor on a daughter board of the ALIBAVA system, with its beetle channels bounded to the sensor strips. The sensor is placed in isolated conditions thanks to a cooling box or similar. The radioactive source is placed on a collimator, over the sensor, at a distance of some centimetres from it. This way, the electrons produced during the decay go through the collimator opening and reach the sensor surface as a beam.

3.4 Infrared laser setup

Infrared laser light is quite piercing in silicon, so for this type of electromagnetic radiation, the sensor behaves like a transparent medium. This kind of source makes possible a high rate fast top-bench characterisation because it does not demand a complex setup, the measurements are done in a short period of time and the number of events that are registered is quite high.

A scan of the high voltage using an iLGAD subject to an infrared laser, with wavelength of 1062 nm, was done in the clean room of IFCA. In order to perform it, the iLGAD and laser were placed inside a dark enclosure, to eliminate external light.

The laser signal is registered by an oscilloscope which showed the sent signal to the iLGAD, and also to a controller which allows the user to select the intensity and pulse duration of the laser signal.

The measurement system, which recorded the signal from the iLGAD, was composed of a computer, an ALIBAVA motherboard, a voltage source for the motherboard, a daughterboard (placed inside the enclosure) and a detector bias source meter.

3.5 Signal Reconstruction

A mip traversing a sensor produces a charge signal which is digitized by the readout electronics in units of ADC counts. This ADC count number, which constitutes the raw data, has three contributions: pedestal, common mode shift and signal. This magnitude is defined for each strip of the sensor and each measured event. Figure 3.5 shows an example of the unprocessed raw data seen by each channel of the setup where only 45 channels are bounded: from 28 to 72. In order to get the signal due only to the mip or incident radiation, the pedestal and noise contributions must be subtracted.

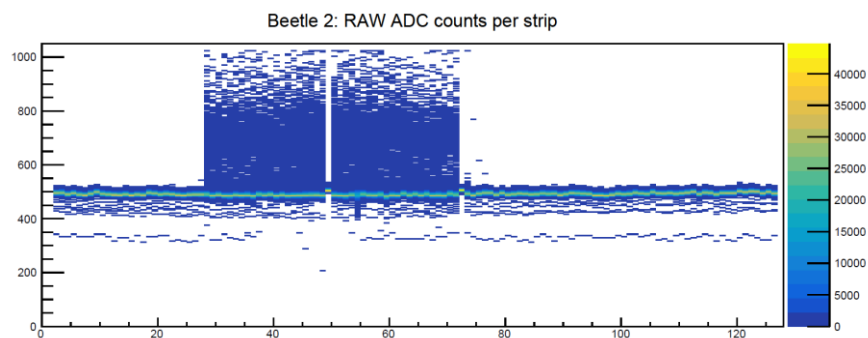


Figure 3.5. Example of the measured ADC counts for 128 channels of the beetle chip. The iLGAD sensor is connected to channels 28 to 72. This measurement is made at 200 V and room temperature.

As before mentioned, the ADC digitizer has 10 bits, which means that it can only read between 0 and 1024 ADC counts, as the vertical axis of Figure 3.5 shows.

The pedestal is the average of measured ADC counts when there is no signal as input. The electronics set a pedestal, the 'zero reference' at approximately the middle of the total ADC range (1024) so it is around 512 ADC counts. This way positive and negative signals can be read.

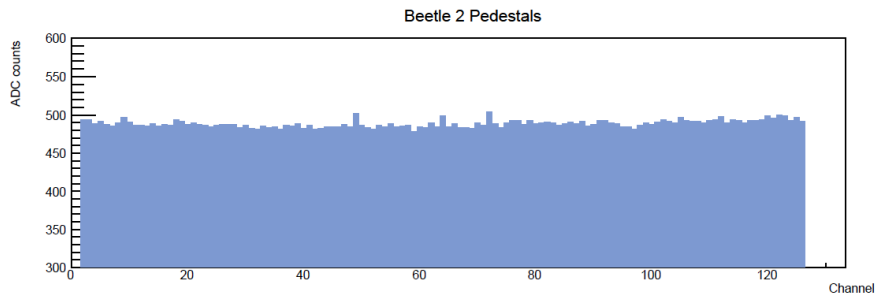


Figure 3.6. Measured pedestals for all 128 channels of the beetle chips in ADC counts.

Also a measurement of the pedestals is carried out before taking data at the same operating conditions, but without any incident radiation on the sensor. The measured pedestals are relatively uniform for all electronic channels, as shown in Figure 3.6. This reference value has to be subtracted from the raw data, so the signal is obtained.

In each event, the signal can be modified by a shift which affects all the channels. This is the common mode shift or common noise and it is an upward or downward fluctuation induced by external noise which affects all channels simultaneously and varies with time and number of event. An example of this type of noise as a function of time (or equivalently event number) is shown in Figure 3.7 together with its projection on the ADC counts axis.

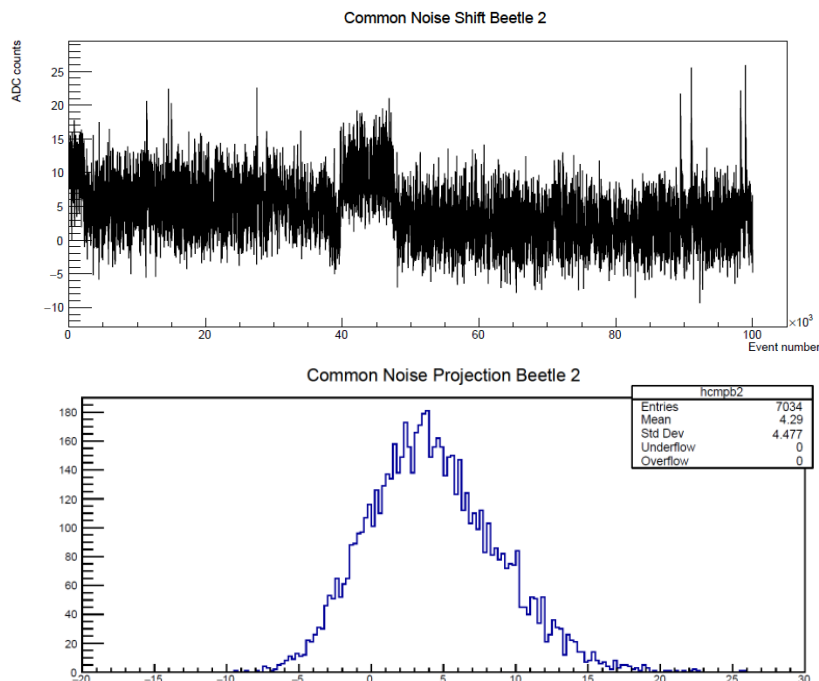


Figure 3.7. Example of a common noise distribution in ADC count units as a function of the event number of an iLGAD measurement at 200 V and room temperature (top). The projection on vertical axis (bottom).

Consequently, subtracting the pedestals and common noise to the raw data, the main signal is obtained, in terms of ADC counts. So ‘Signal’ represents the signal due to the particle convoluted with the intrinsic electronic noise for each channel [19].

$$\text{Signal} = \text{RAWdata} - \text{Pedestal} - \text{CommonNoise}$$

However, each channel i presents its own noise component which is calculated as the RMS (root mean square) of the common noise subtracted pedestal distribution $P_c(i)$, as indicated in Eq. (9).

$$\text{Noise}(i) = \sqrt{\frac{1}{N-1} \sum_{k=1}^N (P_c(i) - \bar{P}_c(i))^2} \quad (9)$$

This distribution has a Gaussian form, as shown in Figure 3.8 for one particular channel, and its width corresponds to the noise for each channel. In this example, the noise is about 3.4 ADC counts.

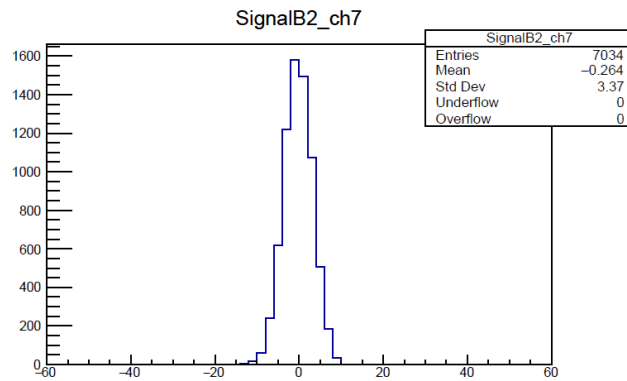


Figure 3.8. Example of a noise distribution in ADC counts for one channel (number 7) of an iLGAD measurement at 200 V.

Those channels which present a signal significantly higher than the noise are said to have hits. A hit is mathematically discerned from the rest of the signal because it has a signal to noise ratio greater than 5. Any channel which has a hit is considered as a seed for a ‘cluster’.

Channels neighbouring a seed which have a signal to noise ratio bigger than 3 are added to the cluster. Consequently a cluster is a group of neighbouring channels with especially high signal significance.

In order to make possible the conversion of the data from ADC counts (what is read) to number of electrons (which has a real physical sense), a calibration measure is done. A specialised calibration circuit injects known amounts of electrons in different steps and the ADC response is recorded, so the resulting equivalence between ADC counts and electrons can be determined from the slope of resulting distribution, as shown in Figure 3.9 for one particular channel.

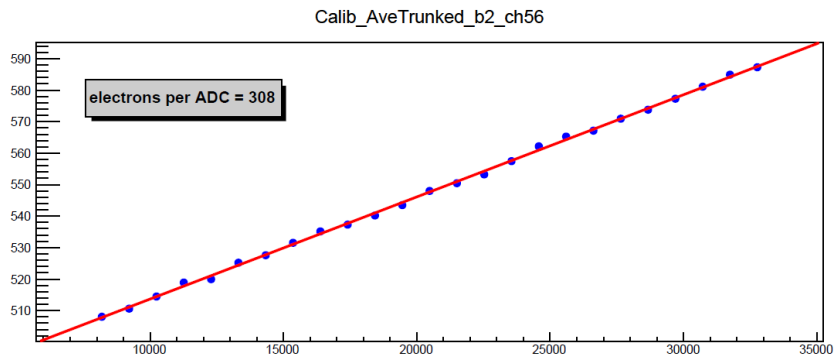


Figure 3.9. Example of a calibration regression for one channel, where the slope is the calibration factor (308 electrons per ADC count).

When representing the calibration factor of all channels, a distribution like Figure 3.10 is obtained.

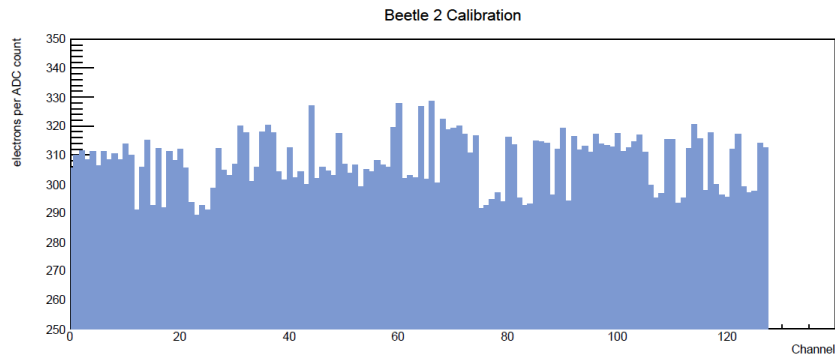


Figure 3.10. Distribution of all channel calibration factors. Bounded channels are distinguished between 28 and 72.

Once the calibration factor has been obtained, the calibrated charge registered by each cluster can be represented, as in Figure 3.11, where only the bounded channels have a cluster and its charge is given in number of electrons. This is the signal due to the incident radiation. The cluster centroid is calculated as the charge-weighted channel number average.

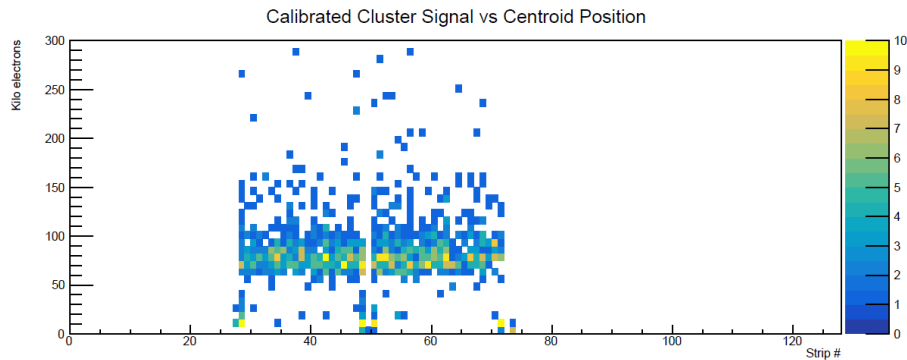


Figure 3.11. Distribution of the calibrated signal of each cluster as a function of the centroid of the cluster.

Finally, from this plot the calibrated charge profile is obtained from the projection on the vertical axis. This distribution, which is shown in Figure 3.12, is fitted to a Landau function convoluted with a Gaussian. The position of the peak of this function represents the most

probable value for the number of electrons generated by the ionizing radiation. This value constitutes the most important information: the collected charge of the sensor due to ionizing radiation for different operating voltages and temperatures.

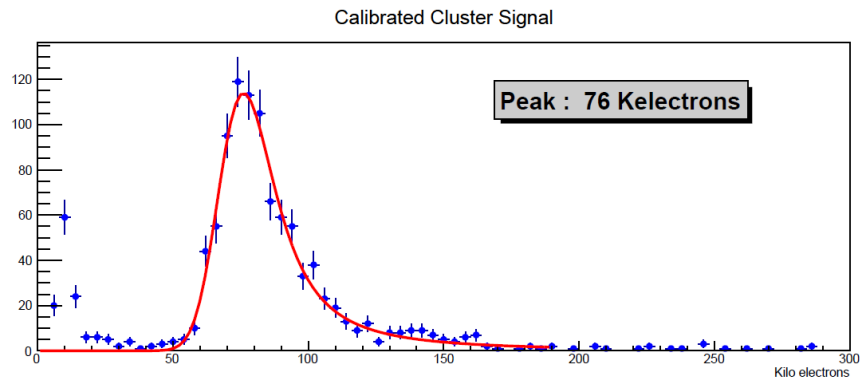


Figure 3.12. Calibrated cluster charge distribution given in kiloelectrons. This is the projection on the vertical axis of Figure 3.11. The red line is the result of the Landau with Gaussian fit.

3.6 Calibration

In relation to the calibration, a dependence study with voltage has been done. On the left of Figure 3.13, the value of the calibrated charge has been obtained running the analysis code using calibration data at similar values to the data measurement. On the right, all the results were obtained with the same unique calibration data which was measured at 200 V. Both plots are exactly the same, so calibration does not depend on voltage.

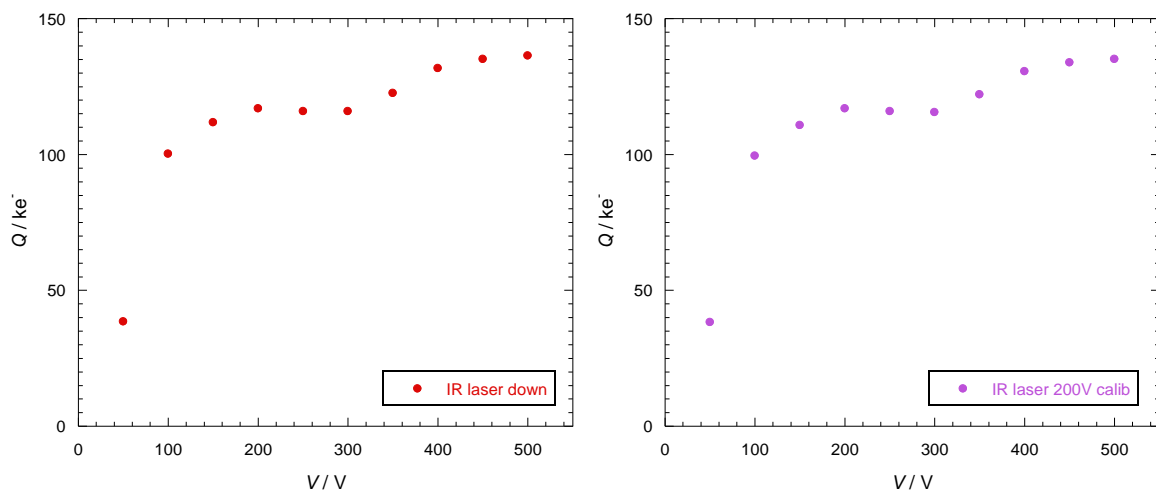


Figure 3.13. Charge measured Q in terms of voltage V using IR laser, illuminating iLGAD from its bottom part at room temperature. The units are kiloelectrons and volts.

- a) When processing data, four different calibration files (100 V, 200 V, 300 V and 400 V) were used.
- b) When processing data, only 200 V calibration file for all the data was used.

In order to widen this calibration study, the calibration factors at different temperatures and voltages are compared in Figure 3.14.

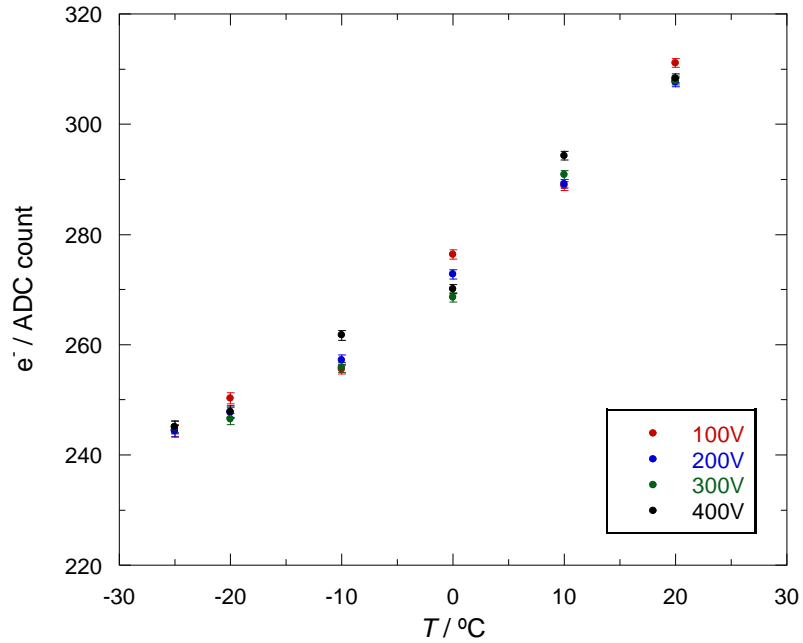


Figure 3.14. Calibration factor comparison for six temperatures and four voltages. Error is displayed with vertical bars.

As can be deduced from Figure 3.14, the calibration is not affected by the voltage value. On the other hand, temperature definitively affects the calibration factor. This indicates how important it is to take calibration runs at the same temperature used to measure the sensor, while the voltage bias does not play a significant role for calibrations.

Finally, we take a quick look at charge distribution between strips. Because of the shape of the electric field inside the sensor, the charge is usually not uniformly distributed but tends to peak near the strips. In order to check how charge is distributed between two consecutive strips, a study with the clusters of size two has been done. The η function has been calculated as the charge fraction on each strip as Eq. (10) shows.

$$\eta = \frac{Q_L}{Q_L + Q_R} ; \quad (10)$$

where Q_L represents the part of the charge which is registered by the strip on the left and Q_R the corresponding to the one on the right. This way, in Figure 3.15, which shows this function from the clusters composed by two strips, values around 1 mean that the strip on the left collects the main part of the charge, while values close to 0 indicate the opposite. As expected, the distribution is not uniform.

It is important to notice that the obtained peaks are not symmetric, due to the fact that incidence of Test Beam particles was not exactly perpendicular to the sensor, due to a small misalignment.

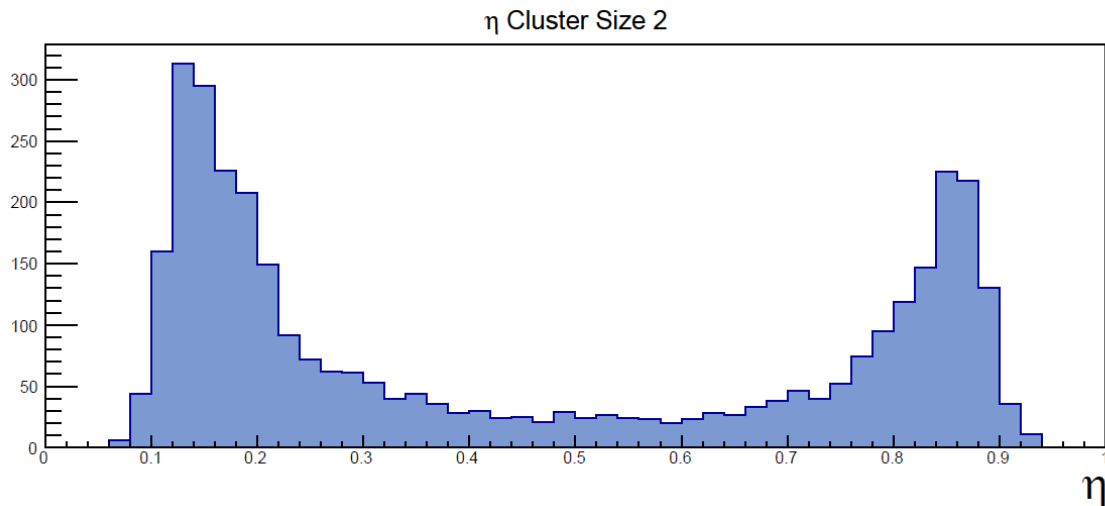


Figure 3.15. Distribution of the η function for all size 2 clusters.

3.7 Data processing codes

In order to process the raw data files which the readout system provides, a ROOT program created with the programming language C is used. This program runs with a steering file which imports three files, each one collecting necessary information differently structured: the data, the pedestals and the calibration for each measurement.

At the end of the process, a PDF file with several graphs is created. It contains information such as temperature of the sensor; pedestals, RAW ADC counts, common noise, signal, noise, signal to noise ratios, hits, clusters, among many other plots which show any information of the iLGAD. All the results shown in this final project have been obtained from the generated plots.

Some code modifications were made, like the automation fitting code. This extra part finds the best range for fitting distributions. The way to do it is the following: it finds the position of the maximum and looks over both sides from it choosing several range values, trying several fits and comparing χ squared values. It works in parallel, doing the calculation more efficient.

Chapter 4:

Characterisation results and discussion

In order to test and verify the applicability of LGADs and iLGADs, a deep study of their characteristics and response to different voltages or types of radiation has been done. These are the first working strip detectors with integrated gain and therefore a characterisation of the gain is the most important achievement of this work.

Depending on the kind of radiation the sensor detects, its signal is quite different, due to its absorption capacity and amount of electron-hole pairs produced. Using an ionizing particle with high energy, like a pion from a beam accelerated to almost light velocity; a less energetic particle from a radioactive source, like ^{90}Sr ; and a photon from an infrared laser, LGADs and iLGADs are characterised throughout this chapter.

In the first part of this chapter, the main results from Test Beam, radioactive source and infrared laser are shown, ending with a comparison between them. Finally, a calibration study is included.

4.1 Test Beam

In Test Beam, the incident particles of the beam were 60% pions and 40% protons, with an energy of 120 GeV. The data taken during Test Beam have been analysed and from the resultant plots it has been possible to extract information related to the charge collection as a function of the applied voltage.

Figure 4.1 (top) shows the calibrated signal as a function of the cluster centroid position, calculated as explained in Section 3.5, for a bias voltage of 200 V. As expected, the clusters populate only the channels which are connected to an iLGAD strip. It is interesting to notice how the sensor was not perfectly aligned during data taking process. From the figure, it seems evident that the beam was pointing towards the right edge of the sensor. In ideal conditions, the beam should have illuminated the centre of the sensor, which would result in higher statistics but it does not affect the distribution of collected charge. The projection on the vertical axis is shown in the bottom figure, fitted with a Landau-Gaussian function with a most probable value (MVP) of 76 kiloelectrons. Four values of bias voltage were applied to an iLGAD at room temperature: 100 V, 200 V, 300 V and 400 V. The MVPs of the calibrated collected charge due to the mips for each bias is represented in Figure 4.2. As can be seen, the measured number of electrons increases with voltage rapidly at low voltages and seems to saturate when reaching high values.

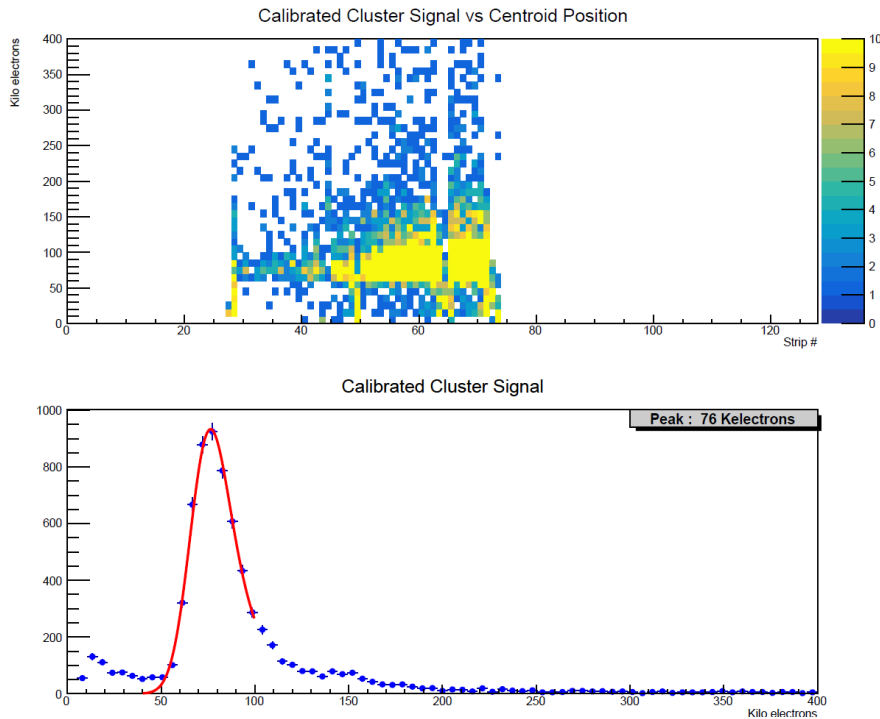


Figure 4.1. Calibrated charge measured with iLGAD at Test Beam, at 200 V.

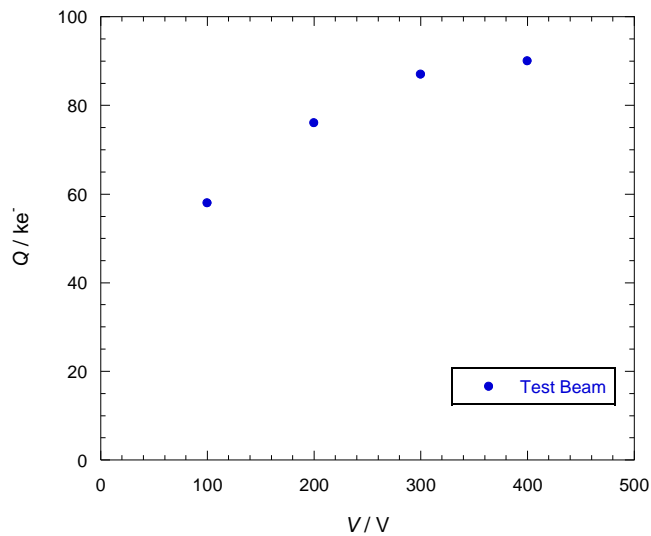


Figure 4.2. Charge Q measured as a function of bias voltage V for Test Beam pions and protons on iLGAD, at room temperature. The units are kiloelectrons and volts, respectively.

Recall that a mip traversing 285 μm of Silicon generates on average a charge of about 23000 electrons (80 electron-hole pairs per micron). However, from Figure 4.2 it can be deduced that for an iLGAD this value is significantly higher owing to the fact that these sensors have an intrinsic gain.

The function of the reference sensor is to make possible measuring this gain by comparing it with the iLGAD. This sensor has 128 channels, the same as the beetle of the frontend of the ALIBAVA. This way, all the measured channels record signal from the radiation. Figure 4.3 shows the measured charge as a function of the cluster position (top) and the number of times each charge value has been measured (bottom).

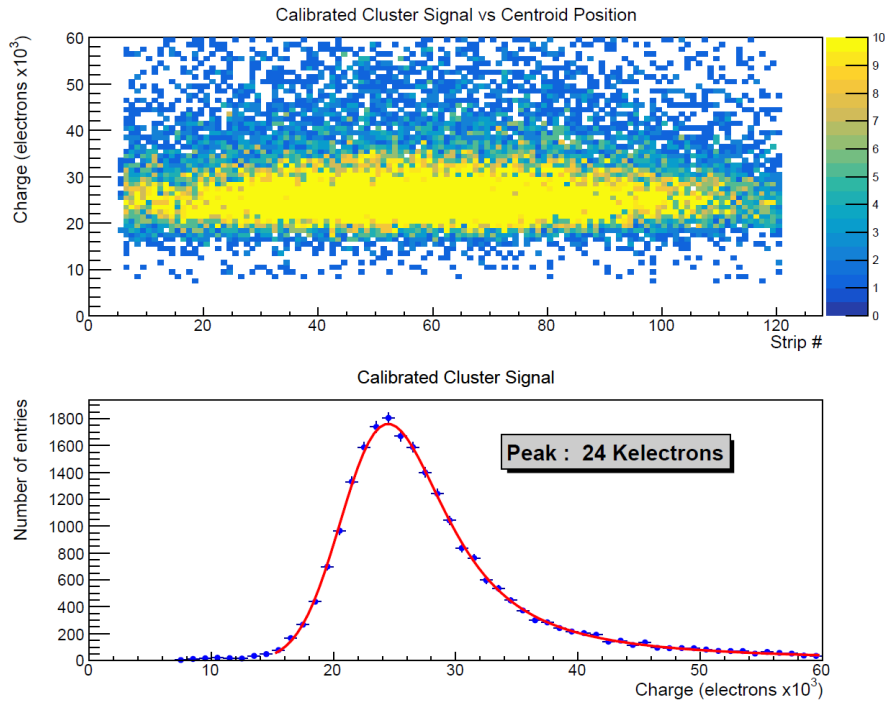


Figure 4.3. Reference sensor at 200 V and 20°C. Calibrated cluster charge versus cluster centroid (top). Projection on the vertical axis (bottom).

Figure 4.3 (bottom) shows the distribution of the measured charge. The position of the maximum value indicates the most probable value of the charge due to the radiation: 24 ke⁻, as expected since the reference sensor has a width of 300 μm . This sensor does not have any gain, so the collected charge is expected to be constant with bias voltage once the sensor is completely depleted.

The gain is estimated as follows:

$$G = \frac{Q_{iLGAD}}{Q_{ref}} \cdot \frac{d_{ref}}{d_{iLGAD}} ; \quad (11)$$

where Q refers to collected charge and d to the thickness of each sensor. Figure 4.4 shows the gain as a function of bias voltage.

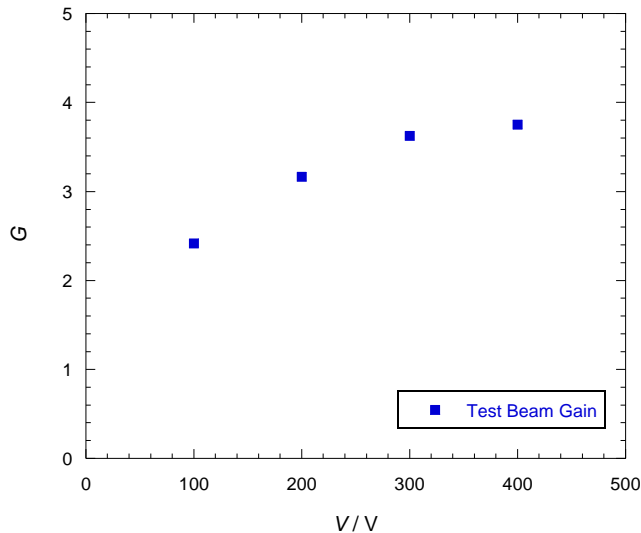


Figure 4.4. Gain G of an iLGAD sensor as a function of bias voltage, at Test Beam.

The gain of the sensor depends on the applied bias, and saturates around 3.5. Consequently, the signal at iLGAD has been intrinsically increased by this factor. The linear increase of collected charge (or equivalently gain) as a function of voltage is probably due to the resistivity of the bulk.

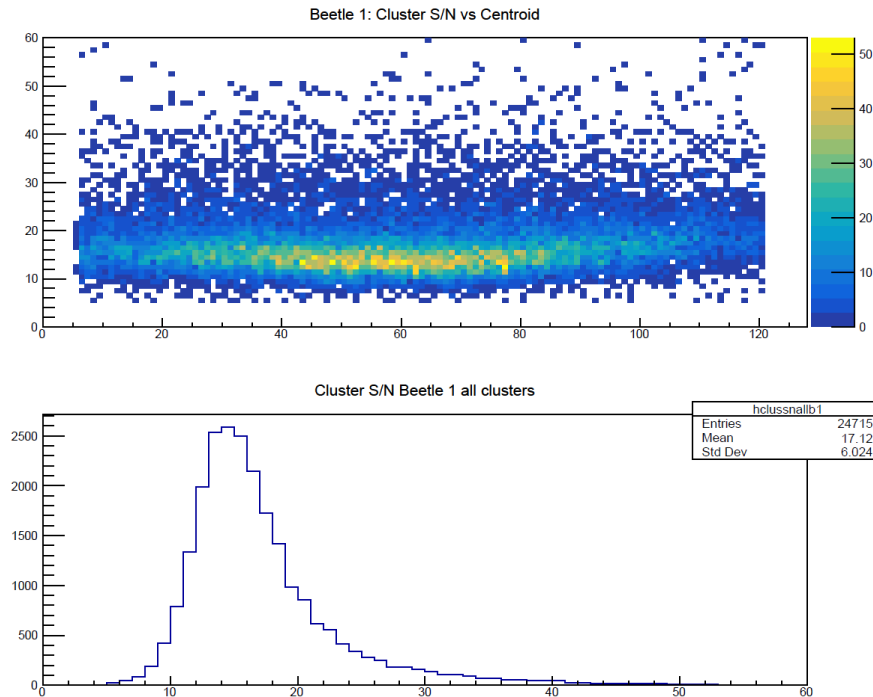


Figure 4.5. Cluster signal to noise as a cluster centroid function (top). Projection on the vertical axis (bottom). Test Beam result of the reference sensor at 200 V and 20°C.

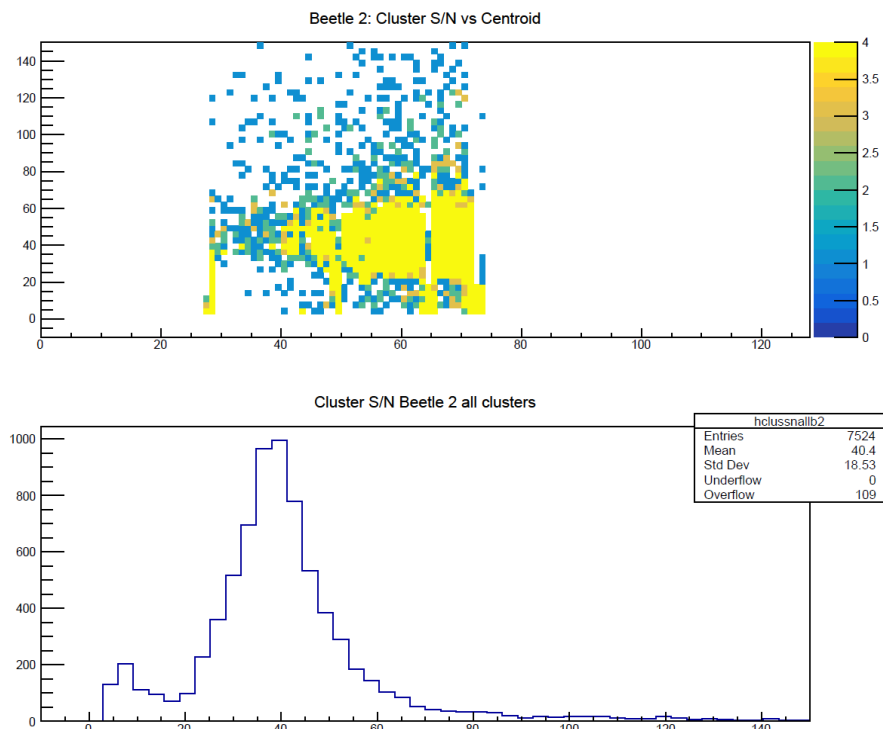


Figure 4.6. Cluster signal to noise as a cluster centroid function (top). Projection on the vertical axis (bottom). Test Beam result of an iLGAD at 200 V and 20°C.

For tracking purposes, a critical quantity for silicon detectors is the signal to noise ratio which quantifies how easily one can distinguish the signal due to the hits from the noise. The distribution of the signal to noise ratio for an iLGAD measurement at 200 V is shown in Figure 4.6. Typical values are between 40 and 60, significantly higher than for standard silicon detectors. This result can be compared with the reference sensor in Figure 4.5, where this value is about 17, a factor of about 2.4 lower than iLGAD.

On the other hand, an LGAD study at Test Beam has been done. Figure 4.7 shows the calibrated charge distribution for an LGAD at -175 V, where an important difference with iLGAD can be detected: there are two main charge peaks instead of one. This fact is due to the LGAD structure which has a segmented multiplication layer. Electron-hole pairs due to mips which traverse the sensor far from the P^{++} multiplication implants never see a high enough electric field and do not multiply. The lowest peak (identified in the figure as Peak 1) is due to these charges so the amount of collected electrons is lower; and Peak 2 is the equivalent to the one which appears in the charge distribution of the iLGAD, coming from multiplied charges.

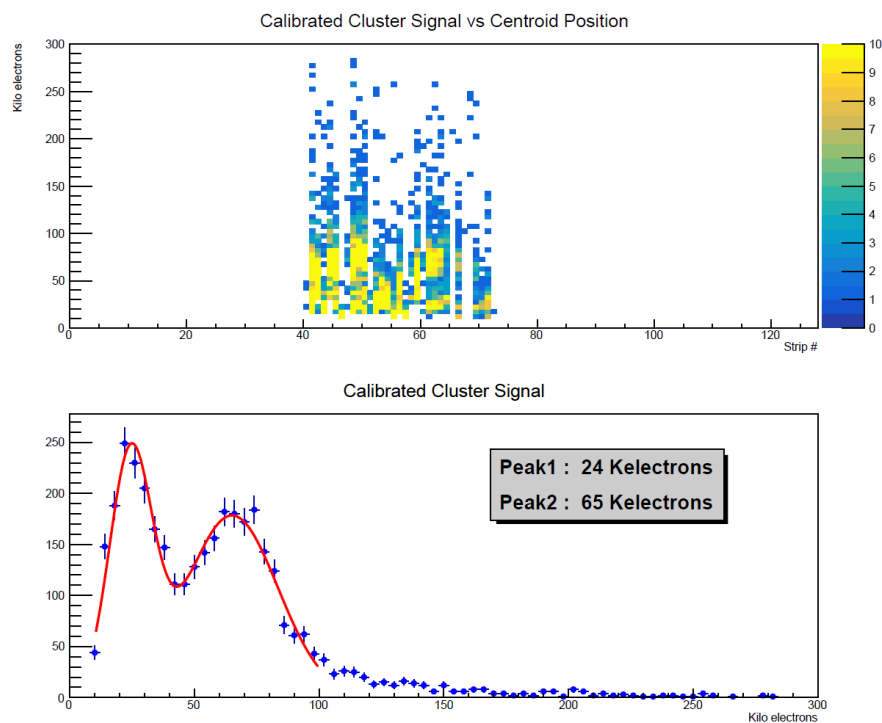


Figure 4.7. Calibrated charge distribution of an LGAD at Test Beam and applying a -175 V bias.

Peak 2 should change with voltage, as collected charge does in an iLGAD because of multiplication increase with bias; while Peak 1 remains constant and it only depends on the width of the sensor once it is fully depleted. In order to check this behaviour, Figure 4.8 shows the dependence of both peaks as a function of the absolute value of the applied voltage. In this figure, the value of Peak 1 remains at 24 ke⁻, for each voltage between -100 and -200 V. The peak due to multiplication presents a larger value and an

increasing behaviour as expected, but the collected charge at similar voltages is slightly lower than the iLGAD, which means this sensor has smaller gain than iLGAD.

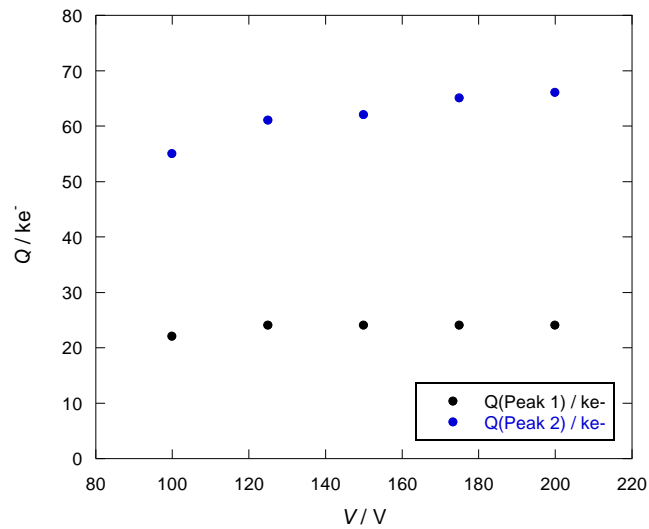


Figure 4.8. Calibrated charge dependence with voltage of an LGAD at Test Beam. Peak 2 represents the charge due to multiplication and Peak 1 without it. The applied voltages are expressed in absolute values.

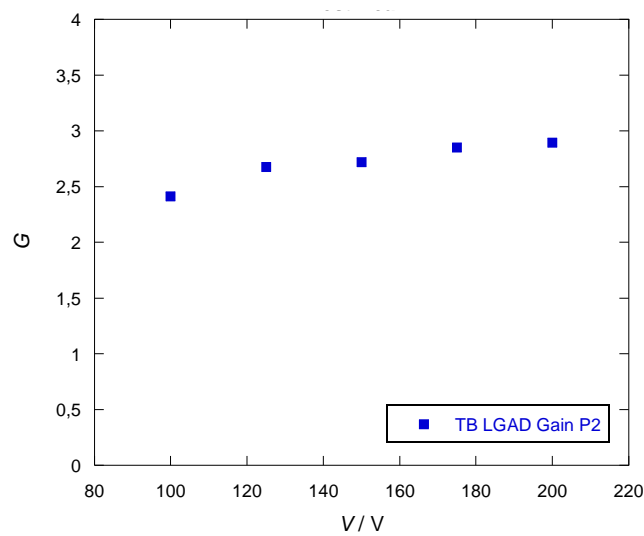


Figure 4.9. Gain G of an LGAD sensor as a function of bias voltage, at Test Beam. This data is a result from the calibrated charge of peak 2, represented as P2.

Figure 4.9 shows that the gain of the LGAD is placed between 2.5 and 3, less than the 3.5 value of iLGAD.

4.2 Radioactive source

The data taking process is simpler than Test Beam and the required infrastructure is easier to get when using a ^{90}Sr radioactive source in order to characterise sensors, as shown in chapter 3. Moreover, the way the sensors are radiated here is quite similar, although the reached energies are several orders of magnitude lower (about 546 keV as maximum against 120 GeV at Test Beam). In Figure 4.10 the measured charge in kiloelectrons of an iLGAD sensor is shown for the different voltage values.

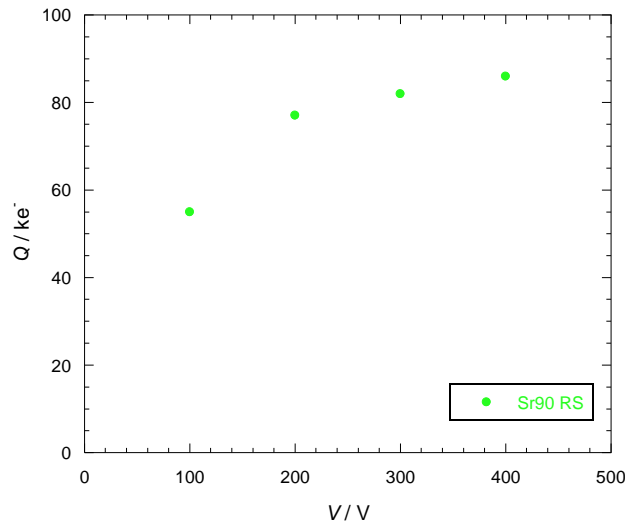


Figure 4.10. Charge Q measured as a function of bias voltage V for radioactive source on iLGAD at room temperature. The units are kiloelectrons and volts, respectively.

Using radioactive source, the relation between the measured charge and applied bias voltage is quite similar to the obtained with Test Beam.

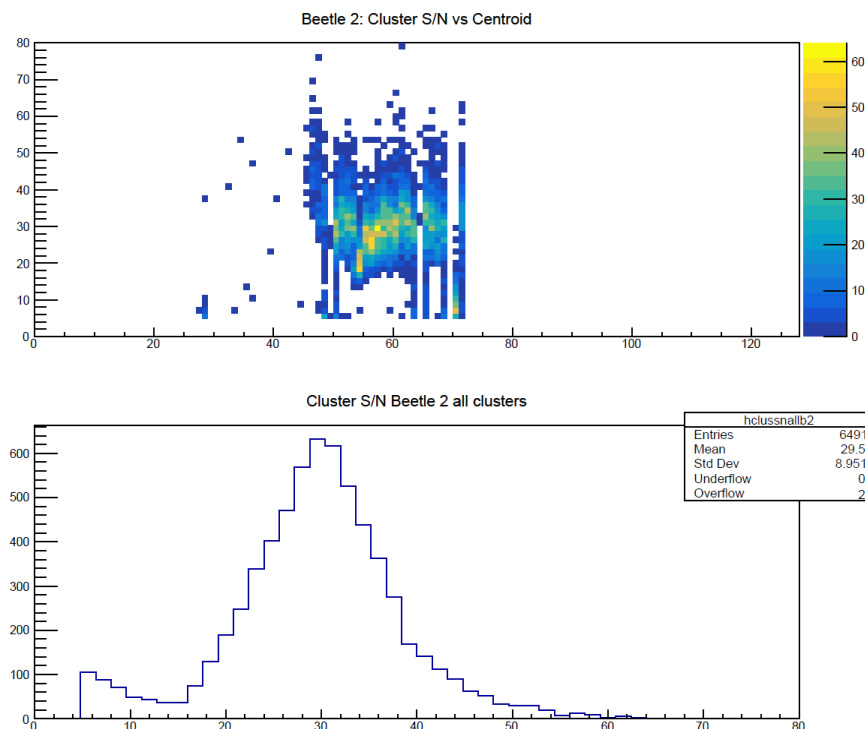


Figure 4.11. Cluster signal to noise as a cluster centroid function (top). Projection on the vertical axis (bottom). ^{90}Sr radioactive source on iLGAD at 300 V and 20°C result.

In order to compare with Test Beam, Figure 4.11 shows the distribution of the signal to noise ratio of each cluster, for a measurement with an iLGAD at 300 V and 20°C.

Comparing top Figures 4.6 and 4.11, it is visible how the illuminated strips of the sensor are different with each source: the position of the measured signals is different for the same bounded channels.

On the other hand, using an LGAD, the calibrated charge distribution for a -150 V voltage is shown in Figure 4.12, where the two charge peaks, as in Test Beam, are distinguished although they are less differentiated. This is because of a geometrical effect since the radioactive source emits in all directions and the incident particles are less collimated, resulting in a large spread of incidence angle. Particles with a big angle of incidence can create electron-hole pairs, some of which drift to the multiplication region while others do not, widening both peaks.

Moreover, the measured calibrated charge of both peaks is represented in Figure 4.13 for different voltages in absolute value.

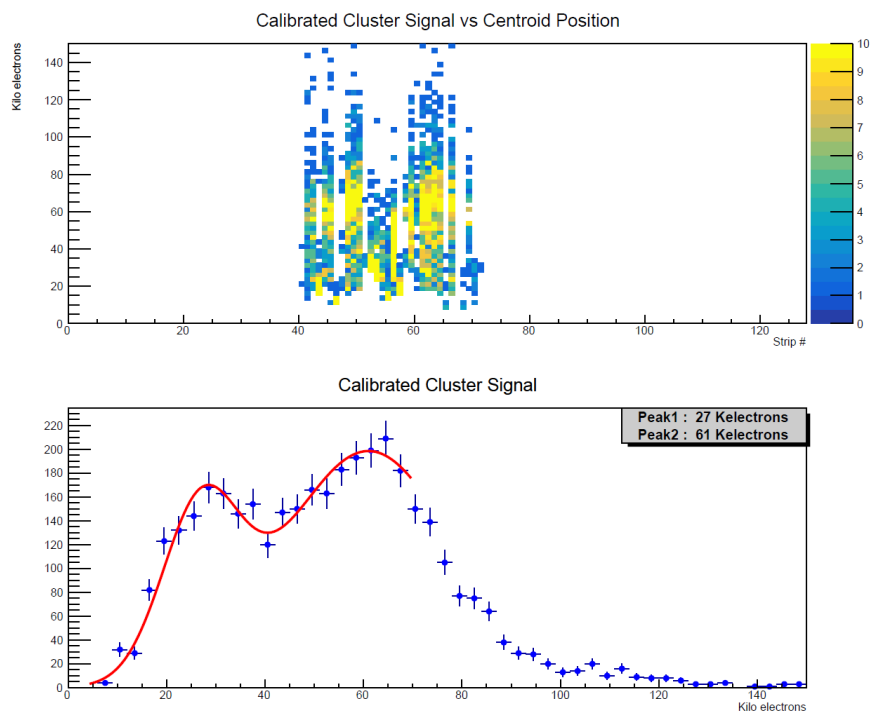


Figure 4.12. Calibrated charge distribution of an LGAD with radioactive source, applying a -150 V bias.

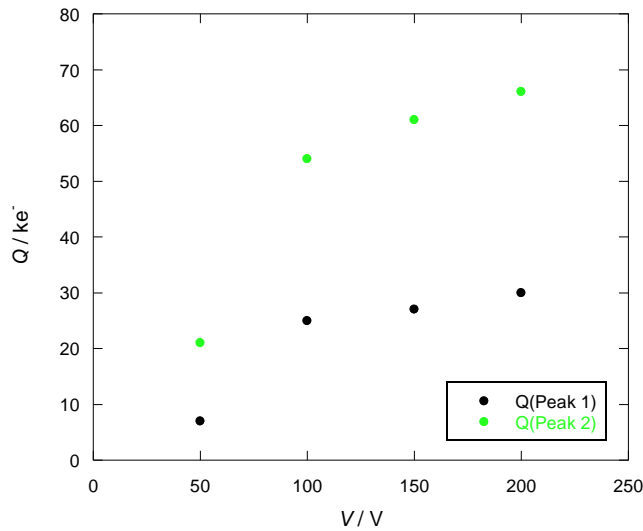


Figure 4.13. Charge Q measured as a function of bias voltage V for radioactive source on LGAD at room temperature. The units are kiloelectrons and volts, respectively.

In this case, for a -50 V applied bias, the obtained charge of both peaks is quite low in comparison with the other voltages. This fact is due to the sensor not being fully depleted, while for 100 V and higher the charge of peak 1 remains fairly constant, as was the case for Test Beam.

After processing the data from the reference sensor with radioactive source at 0 V (see Figure 4.14), its calibrated charge is obtained: around 23.3 kiloelectrons, a quite similar result to the one from Test Beam. This result indicates that reference sensor is responding equally to both sources. The gain of the LGAD when illuminating with radioactive source is obtained with this datum and it is shown in Figure 4.15.

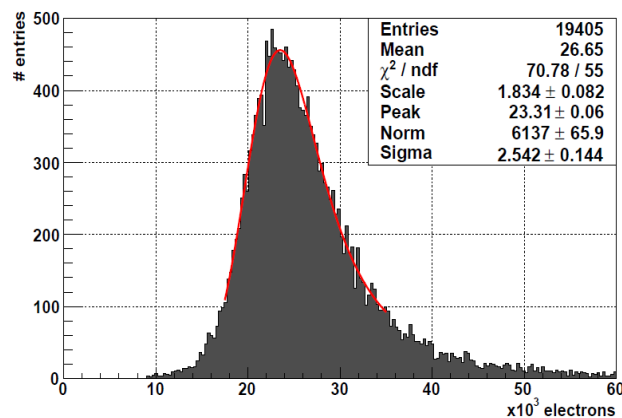


Figure 4.14. Calibrated charge measured by the reference sensor with radioactive source at 0 V.

From Figure 4.15 is deduced that the gain for the LGAD with radioactive source is around 2.5, so it is very similar to the result obtained in Test Beam, as expected due to the fact that it should not depend on the nature of the incident radiation.

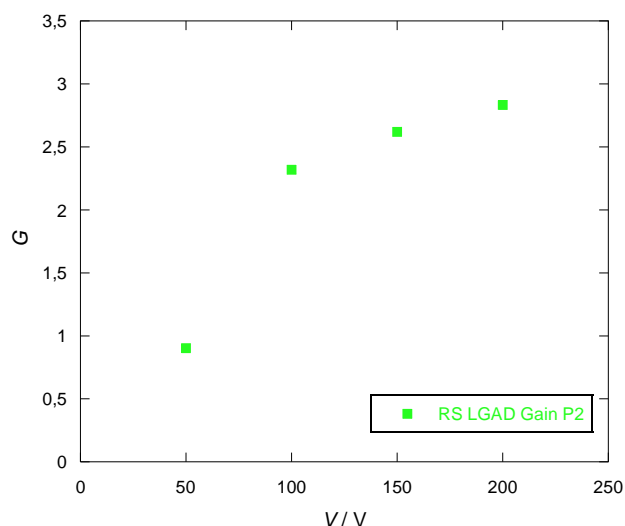


Figure 4.15. Gain G of an LGAD sensor as a function of bias voltage, with radioactive source.

4.3 Infrared laser

In this section the sensor response to photons is tested using an infrared laser. As before mentioned, for red laser silicon is almost opaque, so it does not penetrate more than a few microns. The infrared laser used in this work has a wavelength of 1067 nm. The absorption depth in silicon for photons of this wavelength is around 1 mm, so the laser traverses the entire width (285 μm) of the sensor, similar to a mip. This is the reason why it constitutes another way of characterising sensors, subjecting them to similar conditions as the ones they are expected to work at. The principal advantages of the laser data taking system are that it is cheaper, safer and less complex so measurements are easy and fast to do, obtaining high statistics for each measurement.

The procedure followed in order to make the measurements was the following.

The first thing to do is to tune the laser, to obtain a short pulse while maintaining a relatively low intensity. Next, the distance between the laser and iLGAD is optimized, in order to place the sensor at the focal distance of the laser and produce the narrowest possible spot. Another important step consists on finding the strips where signal is highest, this means, where the laser is mainly impacting.

Once the laser is centred on a strip, we record the strip number and start to save data. Starting with the highest voltage possible (500V), selected in the detector bias, and writing down the corresponding electric current intensity, the software saves the data in a text document.

Selecting different voltages from 500 V to 50 V, in steps of 50 V, the measurement process was completed.

As done in the previous sections, the measured charge in kiloelectrons for different voltages can be found in Figure 4.16, in order to see the response of the sensor, depending on the applied bias.

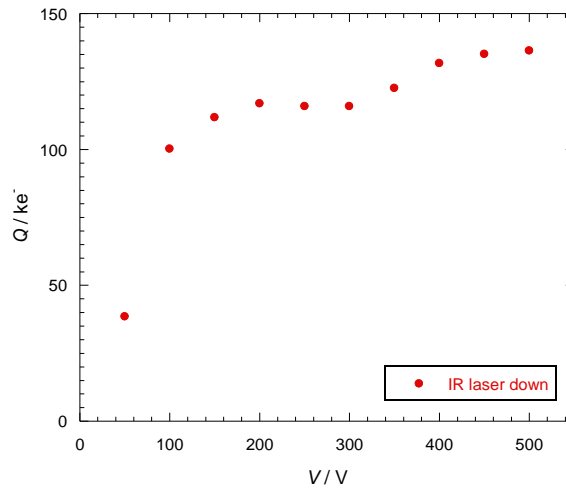


Figure 4.16. Charge measured Q in terms of voltage V using IR laser, illuminating iLGAD from its bottom part at room temperature. The units are kiloelectrons and volts.

The response is similar to that obtained with Test Beam and radioactive source. The kink observed in Figure 4.16 is most likely due to laser intensity instabilities with time during the data taking process.

For the LGAD sensor, which has a segmented multiplication layer, it is interesting to perform an infrared laser scan across strips, which consists on recording the charge as a function of the position of the sensor. For this particular study, only three strips were directly connected to an oscilloscope (the ALIBAVA setup was not used), and the signal recorded by each of the three oscilloscope channels was recorded in arbitrary units.

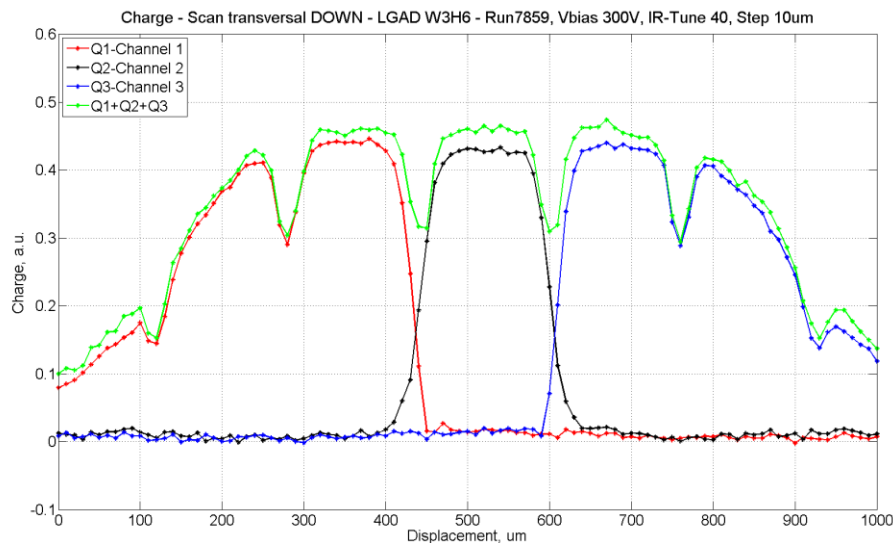


Figure 4.17. Charge measured in terms of surface sensor position, using IR laser illuminating LGAD from its bottom part, at room temperature and 300 V.

The zones of an LGAD where multiplication takes place can be distinguished from the ones where it does not, using an infrared laser illuminating the bottom part of the LGAD, as shown in Figure 4.17. The registered charged by each channel is represented with red, black and blue, while the sum of them with green. The total contribution of the minimums of green line generates the peak without multiplication in the charge distribution, and the maximums the higher peak.

The centres of the signals of each channel are separated by a distance of 160 μm , which corresponds to the pitch of the sensor, as expected.

4.4 Comparison between radiation sources

Once the response of the sensor to the three radiation sources has been studied, it is essential to compare the results in order to extract conclusions and verify that it is responding as it was expected.

In the first place, it would be expected to see a quite similar response of the charge at Test Beam (TB) and radioactive source (RS), since both are ionizing particles: pions and protons in the first and electrons in the second. Since electrons from the RS are not so energetic, they could in principle generate a slightly larger charge than TB particles on average. A normalization factor is therefore used to compare RS and TB results, and we arbitrarily chose this factor to be the ratio of calibrated charge at 200 V between the two sources. A similar normalization is used between laser and TB, at 200 V, since of course the charge for the laser depends on the laser intensity and does not have to be the same as for a mip.

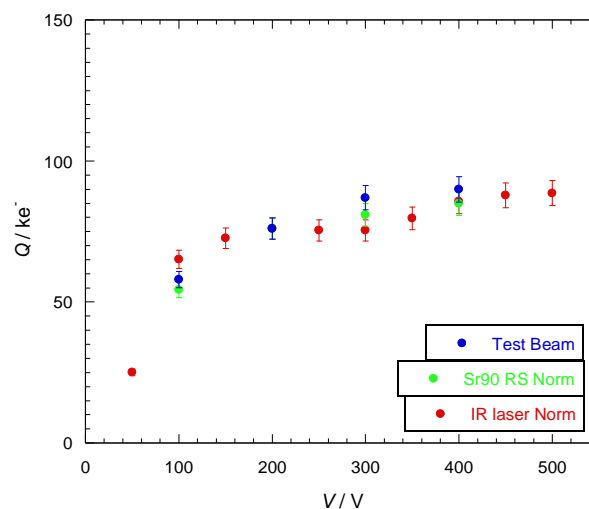


Figure 4.18. Comparison of the charge Q for the iLGAD sensor in terms of voltage V , and normalising to 200 V Test Beam. The units are kiloelectrons and volts. Comparing ^{90}Sr Radioactive Source, Test Beam and IR laser.

Figure 4.18 shows the calibrated charge for all three sources as a function of voltage, for the iLGAD sensor. They all agree perfectly at the 200 V point by the normalization procedure.

Test Beam and radioactive source present quite similar behaviours, presenting compatible calibrated charge. For the IR laser, the trend is similar but values around 300 V might be lower than expected due to a possible downward fluctuation in laser intensity.

The error of each calibrated charge value is around 2 kiloelectrons due to three main contributions: temperature, time window and statistical error. Assuming an error of one degree Celsius in the value of the temperature, and deducing from Figure 3.14 that there is a change of 1.5 ke^- per degree, the temperature contribution of the error is 1.5 ke^- . Furthermore, depending on the chosen time window which is supposed to have a range of a couple of nanoseconds (time in which the incident radiation was more likely to reach the sensor), there is a fluctuation of 1 ke^- when changing it one nanosecond. Finally, the statistical error (from the most probable value of the calibrated charge calculation) is around 0.2 ke^- , insignificant compared with the other two. The squared sum of these errors results in the global error of around 2 ke^- . The error due to the instability of the laser was not studied further and is not considered in Figure 4.18.

Furthermore, when comparing calibrated charge as a function of voltage for an LGAD, with Test Beam and radioactive source, the result is shown in Figure 4.19. Both radiation sources produce quite similar results at the voltages for which they have data in common (100, 150 and 200 V), generating the same charge in the sensor. The data at 125 and 175 V satisfactorily maintain the trend of these three data points.

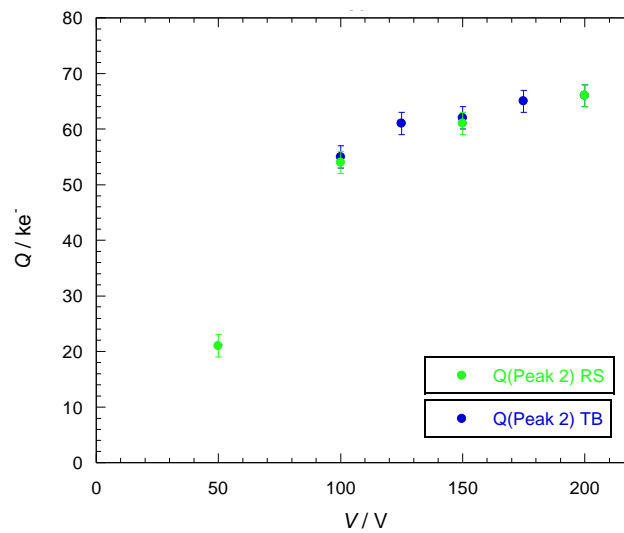


Figure 4.19. Charge comparison between radioactive source and Test Beam for an LGAD at room temperature. The charge is the corresponding to peak 2 in the charge distributions.

The measured calibrated charge at 50 V does not follow the same trend as higher voltage data, which can be explained with a non full depletion of the sensor, whose depletion voltage is around 70 V.

The value of the error bars in this plot has been obtained in the same way as the iLGAD, so the absolute error is around 2 kiloelectrons.

Conclusions and outlook

The work performed along this academic work has been focused on a new type of silicon radiation sensors with integrated gain: LGAD and iLGAD. These detectors arise from the need for quite accurate momentum measurements, fast data taking and sensitive energy detection. These are the first working microstrip silicon detectors with intrinsic gain. In order to verify the versatility and excellent behaviour of these devices, a study of their response to different types of radiation has been performed.

LGAD and iLGAD sensors are quite thin diodes (285 μm) able to register a wide range of energy signals from ionizing radiation thanks to its multiplication layer, which increases low charge collections to measurable values. They can provide good space resolution due to the microstrip configuration of the collector electrodes, good time resolution thanks to their fast response, and an unprecedentedly large signal to noise.

The results of the characterisations of the sensors have been already shown in the figures of Chapter 4, where collected charge, gain and signal to noise are studied as a function of bias voltage for both sensors and for all three radiation sources. Table 1 shows only a selection of these results, where Test Beam is chosen because of the similarity with the sensors applications and the 200 V bias voltage is used since it is the highest bias used for the LGAD. For comparison purposes, the corresponding values of a standard microstrip sensor (with no gain) is also shown.

Sensor	Q (ke^-)	Q/d ($\text{e}^-/\mu\text{m}$)	Gain	S/N
iLGAD	76	270	3.2	40
LGAD	66	230	2.5	17
Reference	24	80	1	17

Table 1. Comparison between total collected charge Q , charge per micron Q/d , gain G and signal to noise S/N of iLGAD, LGAD and reference sensors, for Test Beam and 200 V applied voltage.

This kind of detectors, which are starting to be used in tracking applications, will likely play a decisive role in timing applications, providing the capability to resolve multiple vertices coming from the same collider bunch crossing, by combining spatial and time resolution into a 4D vertexing. Both the CMS and ATLAS detectors at LHC are already considering this technology for timing applications in their high luminosity upgrades.

A very important characterisation which remains to be done in the future is the study of the radiation tolerance of these devices.

References

- [1] The International Large Detector: Letter of Intent. Web page available at:
<https://arxiv.org/abs/1006.3396>
- [2] The SiD Detector for the International Linear Collider. Web page available at:
<https://arxiv.org/abs/1511.00134>
- [3] Review Silicon detector systems in high energy physics. Hans-Gunther Moser. Elsevier
- [4] CMS. Web page available at:
<https://cms.web.cern.ch/org/tracker>
- [5] Activity book for students ALIBAVA systems. Barcelona. Section 2.1 to 2.7. Pg 11-20
- [6] W. R. Leo. *Techniques for Nuclear and Particle Physics Experiments*. Springer-Verlag. 1987. Chapter 10. Pg 207-210
- [7] Crystalline doped structure. Solar journey USA web. Web page available at:
<http://solarjourneyusa.com/bandgaps.php>
- [8] Web page available at:
<http://hyperphysics.phy-astr.gsu.edu/hbase/electric/conins.html>
- [9] Web page available at:
<http://www.radio-electronics.com/info/formulae/resistance/resistivity-basics-formula-equation-units.php>
- [10] M. Balkanski, Richard Fisher Wallis. *Semiconductor Physics and Applications*. Web page available at:
https://books.google.es/books?id=BOWhiKEnoeEC&printsec=frontcover&dq=semiconductor+principles&hl=es&sa=X&ved=0ahUKEwicpaefzu_TAhULCMAKHXQFCccQ6AEIMTAC#v=onepage&q=semiconductor%20principles&f=false
- [11] Image of a diode response. Web page available at:
<https://learn.sparkfun.com/tutorials/diodes/real-diode-characteristics>
- [12] *Diseño fabricación y Optimización de Detectores con multiplicación (LGAD) para experimentos de Física de Altas Energías*. Pablo Fernández Martínez
- [13] G. Pellegrini, P.Fernández-Martínez, M.Baselga, C.Fleta, D.Flores, VGreco, S. Hidalgo, I.Mandić, G.Kramberger, D.Quirion, M.Ullan. *Technology developments and first measurements of Low Gain Avalanche Detectors (LGAD) for high energy physics applications*. Nuclear Instruments and Methods in Physics Research A 765 (2014) 12–16

- [14] I. Vila. *Signal amplification in segmented silicon sensors: strip-LGAD and I-LGAD*. RD50 Workshop, Torino June 6th, 2016
- [15] I. Vila. *Update on the I-LGAD characterization*. RD50 Workshop, CERN November 22th, 2016
- [16] ALIBAVA Systems. Company born from the collaboration of three research institutes: University of Liverpool, UK; IMB-CNM (CSIC), Barcelona, Spain; and IFIC (CSIC), Valencia, Spain; in the field of radiation detectors for Particle Physics applications. Web page available at:
<https://www.alibavasystems.com/>
- [17] S. Löchner and M. Schmelling. *The Beetle Reference Manual for Beetle Version 1.3, 1.4 and 1.5*, LHCb note 2005-105, Aug. 22, 2006 [Online]. Web page available at:
http://fpmac116.usc.es/twiki/pub/Instrumentation/Beetle/Beetle_reference_manual.pdf
- [18] Diagram of CERN accelerators. Web page available at:
<http://cern-accelerators-optics.web.cern.ch/cern-accelerators-optics/>
- [19] Activity book for students ALIBAVA systems. Barcelona. Section 4.2 to 4.8. Pg 41-60